

Structural basis of odorant recognition by a human odorant receptor

<https://doi.org/10.1038/s41586-023-05798-y>

Received: 20 November 2022

Accepted: 6 February 2023

Published online: 15 March 2023

 Check for updates

Christian B. Billesbølle^{1,9}, Claire A. de March^{2,8,9}, Wijnand J. C. van der Velden^{3,9}, Ning Ma³, Jeevan Tewari², Claudia Llinas del Torrent^{1,4}, Linus Li¹, Bryan Faust¹, Nagarajan Vaidehi^{3,✉}, Hiroaki Matsunami^{2,5,✉} & Aashish Manglik^{1,6,7,✉}

Our sense of smell enables us to navigate a vast space of chemically diverse odour molecules. This task is accomplished by the combinatorial activation of approximately 400 odorant G protein-coupled receptors encoded in the human genome^{1–3}. How odorants are recognized by odorant receptors remains unclear. Here we provide mechanistic insight into how an odorant binds to a human odorant receptor. Using cryo-electron microscopy, we determined the structure of the active human odorant receptor OR51E2 bound to the fatty acid propionate. Propionate is bound within an occluded pocket in OR51E2 and makes specific contacts critical to receptor activation. Mutation of the odorant-binding pocket in OR51E2 alters the recognition spectrum for fatty acids of varying chain length, suggesting that odorant selectivity is controlled by tight packing interactions between an odorant and an odorant receptor. Molecular dynamics simulations demonstrate that propionate-induced conformational changes in extracellular loop 3 activate OR51E2. Together, our studies provide a high-resolution view of chemical recognition of an odorant by a vertebrate odorant receptor, providing insight into how this large family of G protein-coupled receptors enables our olfactory sense.

Our sense of smell relies on our ability to detect and discriminate a vast array of volatile odour molecules. The immense chemical diversity of potential odorants, however, poses a central challenge for the olfactory system of all animals. In vertebrates, the vast majority of odorants are detected by odorant receptors (ORs), which are G protein-coupled receptors (GPCRs) expressed in olfactory sensory neurons (OSNs) projecting from the olfactory epithelium to the olfactory bulb in the brain^{1,3}. To detect and discriminate the vast diversity of potential odorants⁴, the OR gene family has expanded dramatically in vertebrate genomes, with some species encoding thousands of OR genes⁵. In humans, the approximately 400 functional ORs constitute half of the broader class A GPCR family^{6–8} (Fig. 1a).

Odorant stimulation of ORs activates signalling pathways via the stimulatory G protein G_{olf} , which ultimately leads to excitation of OSNs⁹. Each OR can only interact with a subset of all potential odorants. Conversely, a single odorant can activate multiple ORs². This principle of molecular recognition enables a central neural logic of olfaction in which the perception of smell arises from the combinatorial activity of multiple unique ORs that respond to an individual odorant². Because each mature OSN expresses only a single OR gene¹⁰, understanding how an individual OR is activated provides direct insight into the sensory coding of olfaction.

To understand olfaction at a fundamental level, we need a structural framework describing how odorants are recognized by ORs. Although

recent structures of insect odorant-gated ion channels have begun to decipher this molecular logic^{11,12}, the molecular rules that govern odorant recognition in vertebrate ORs are probably distinct and remain obscure. Here, we used cryo-electron microscopy (cryo-EM) to determine the structure of a human OR activated by an odorant. This structure reveals specific molecular interactions that govern odorant recognition and provides a foundation for understanding how odorant binding activates ORs to instigate cellular signalling.

Structure of odorant-bound OR51E2

Several challenges have limited structural interrogation of vertebrate ORs, including low expression levels in heterologous systems, low solubility of most volatile odorants and precipitous instability of purified ORs^{13–16}. We therefore sought to identify a human OR that overcomes these challenges. We prioritized a subset of ORs that is also expressed in tissues outside of OSNs with chemoreceptive functions that are independent of olfaction¹⁷. The ability of these ORs to function in non-olfactory tissue suggested that they may be more amenable to expression in heterologous cell expression systems that lack olfactory-tissue-specific chaperones¹⁴. In a second line of reasoning, we prioritized class I (so called fish-like) ORs as these receptors generally recognize water-soluble odorants¹⁸. By contrast, class II ORs tend

¹Department of Pharmaceutical Chemistry, University of California, San Francisco, CA, USA. ²Department of Molecular Genetics and Microbiology, Duke University, Durham, NC, USA.

³Department of Computational and Quantitative Medicine, Beckman Research Institute of the City of Hope, Duarte, CA, USA. ⁴Laboratory of Computational Medicine, Biostatistics Unit, Faculty of Medicine, Universitat Autònoma Barcelona, Bellaterra, Barcelona, Spain. ⁵Department of Neurobiology, Duke Institute for Brain Sciences, Duke University, Durham, NC, USA. ⁶Department of Anesthesia and Perioperative Care, University of California, San Francisco, CA, USA. ⁷Chan Zuckerberg Biohub, San Francisco, CA, USA. ⁸Present address: Institut de Chimie des Substances Naturelles, UPR2301 CNRS, Université Paris-Saclay, Gif-sur-Yvette, France. ⁹These authors contributed equally: Christian B. Billesbølle, Claire A. de March, Wijnand J. C. van der Velden. [✉]e-mail: NVaidehi@coh.org; hiroaki.matsunami@duke.edu; aashish.manglik@ucsf.edu

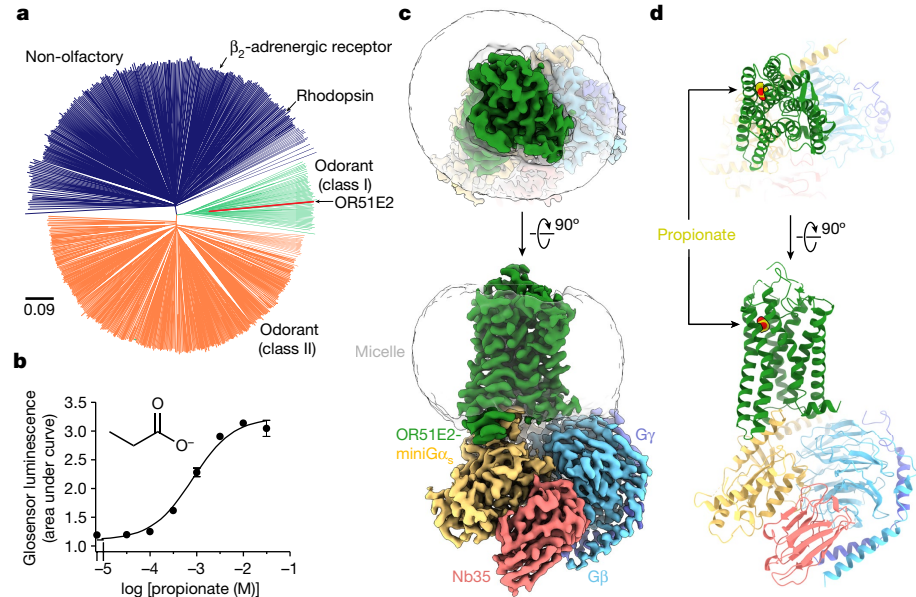


Fig. 1 | Structure of the human OR OR51E2. **a**, Phylogenetic tree of human class A GPCRs, including both non-olfactory and ORs. ORs are further divided into class I and class II. OR51E2 is a class I OR. The phylogenetic distance scale is represented in the left bottom corner (the distance represents 9% differences between sequences). **b**, Real-time monitoring of a cAMP concentration assay showing that human OR51E2 responds to the odorant propionate. Small

vertical line indicates intercept with y-axis ($x=0$). Inset, chemical structure of propionate. Data points are mean \pm standard deviation from $n=4$ replicates. **c,d**, Cryo-EM density map (**c**) and ribbon model (**d**) of active human OR51E2 bound to propionate (yellow spheres). OR51E2 is fused to miniG α_s and bound to both G β and the stabilizing nanobody Nb35.

to respond to more hydrophobic odorants. In addition, class I ORs induce decreased levels of endoplasmic reticulum stress compared with class II ORs¹⁹, and are therefore likely to yield increased expression in heterologous cells. Finally, we prioritized ORs that are conserved across evolution, potentially because they recognize odorants that are critical for animal survival across many species⁵. We reasoned that such ORs may be more constrained by evolution for stability. With this approach, we identified human OR51E2, also known as prostate-specific G protein-coupled receptor, as an ideal candidate for structure determination (Extended Data Fig. 1). OR51E2 is a class I OR that responds to the short-chain fatty acid propionate²⁰ (Fig. 1a,b). In addition to its olfactory function, OR51E2 and its mouse orthologue Olfr78 are expressed in several other tissues to enable chemoreception of short-chain fatty acids^{21–26}. Consistent with our reasoning, OR51E2 emerged as one of the most highly expressed ORs when transiently expressed in HEK293T cells among hundreds of human and mouse ORs that we have previously tested¹³.

To further stabilize OR51E2, we aimed to isolate OR51E2 in a complex with a heterotrimeric G protein. ORs couple with the two highly homologous stimulatory G proteins G α_{olf} and G α_s . In mature OSNs, ORs activate G α_{olf} to stimulate cAMP production via adenyl cyclase⁹. In immature OSNs, ORs activate adenyl cyclase via G α_s outside of the olfactory system in tissues lacking G α_{olf} ²². The ability of OR51E2 to signal physiologically via G α_s , combined with the availability of a nanobody (Nb35) that stabilizes GPCR–G α_s complexes²⁸, prompted us to focus on purifying an OR51E2–G α_s complex. To do so, we generated an OR51E2 construct with a C-terminally fused ‘miniG α_s ’ protein. The miniG α_s protein is engineered to trap the receptor-interacting conformation of G α_s in the absence of any guanine nucleotide²⁹. Fusion of the miniG α_s to OR51E2 fully blocked propionate-stimulated cAMP signalling in HEK293T cells (Extended Data Fig. 2b). We surmised that miniG α_s tightly engages the seven transmembrane (7TM) core of OR51E2 to preclude endogenous G α_s coupling and cAMP production.

We purified OR51E2–miniG α_s in the presence of 30 mM propionate, and then further generated a complex with recombinantly purified

G $\beta_1\gamma_2$ and Nb35 (Extended Data Fig. 2a,c). The resulting preparation was vitrified and analysed by single-particle cryo-EM (Extended Data Table 1 and Extended Data Fig. 3), which yielded a 3.1 Å resolution map of OR51E2 bound to the G α_s heterotrimer. We additionally generated a map with focused refinement on only the 7TM domain of OR51E2, which afforded improved map resolution of the binding site and extracellular loops of the receptor (Extended Data Fig. 3e). The resulting reconstructions allowed us to model the OR51E2 7TM domain, the propionate ligand and the G α_s heterotrimer (Fig. 1c,d and Extended Data Fig. 4a–c).

Odorant-binding pocket

We identified cryo-EM density for propionate in a region bounded by transmembrane helix 3 (TM3), TM4, TM5 and TM6 in OR51E2 (Fig. 2a and Extended Data Fig. 4b,d). The propionate odorant-binding pocket in OR51E2 is in a similar general region as ligand-binding pockets in two prototypical class A GPCRs: the adrenaline-binding site in the β_2 -adrenergic receptor (β_2 AR)³⁰ and all-trans retinal in rhodopsin³¹ (Fig. 2a–c). Compared with the β_2 AR and rhodopsin, the odorant-binding pocket in OR51E2 is smaller and does not engage TM2 and TM7. Extensive packing of the OR51E2 N terminus with extracellular loop 1 (ECL1) and ECL2 diminishes the potential size of the odorant-binding pocket. Of note, unlike many class A GPCRs with difusible agonists, the binding pocket for propionate is fully occluded from the extracellular milieu (Fig. 2d).

Propionate makes several contacts within the OR51E2 odorant-binding pocket. The carboxylic acid of propionate engages R262^{6×59} (superscript numbers indicate generic GPCR numbering following the revised Ballesteros–Weinstein system for class A GPCRs^{32–34}) in TM6 as a counter-ion. The same propionate functional group also engages in hydrogen-bonding interactions with S258^{6×55} and Q181^{45×53} in ECL2 (Fig. 2e). We used molecular dynamics (MD) simulations to understand whether these interactions are stable. We performed five 1-μs simulations of OR51E2 bound to propionate but in the absence of the G α_s heterotrimer. During these simulations, we observed that the carboxylic group of propionate forms a persistent interaction with R262^{6×59}, with

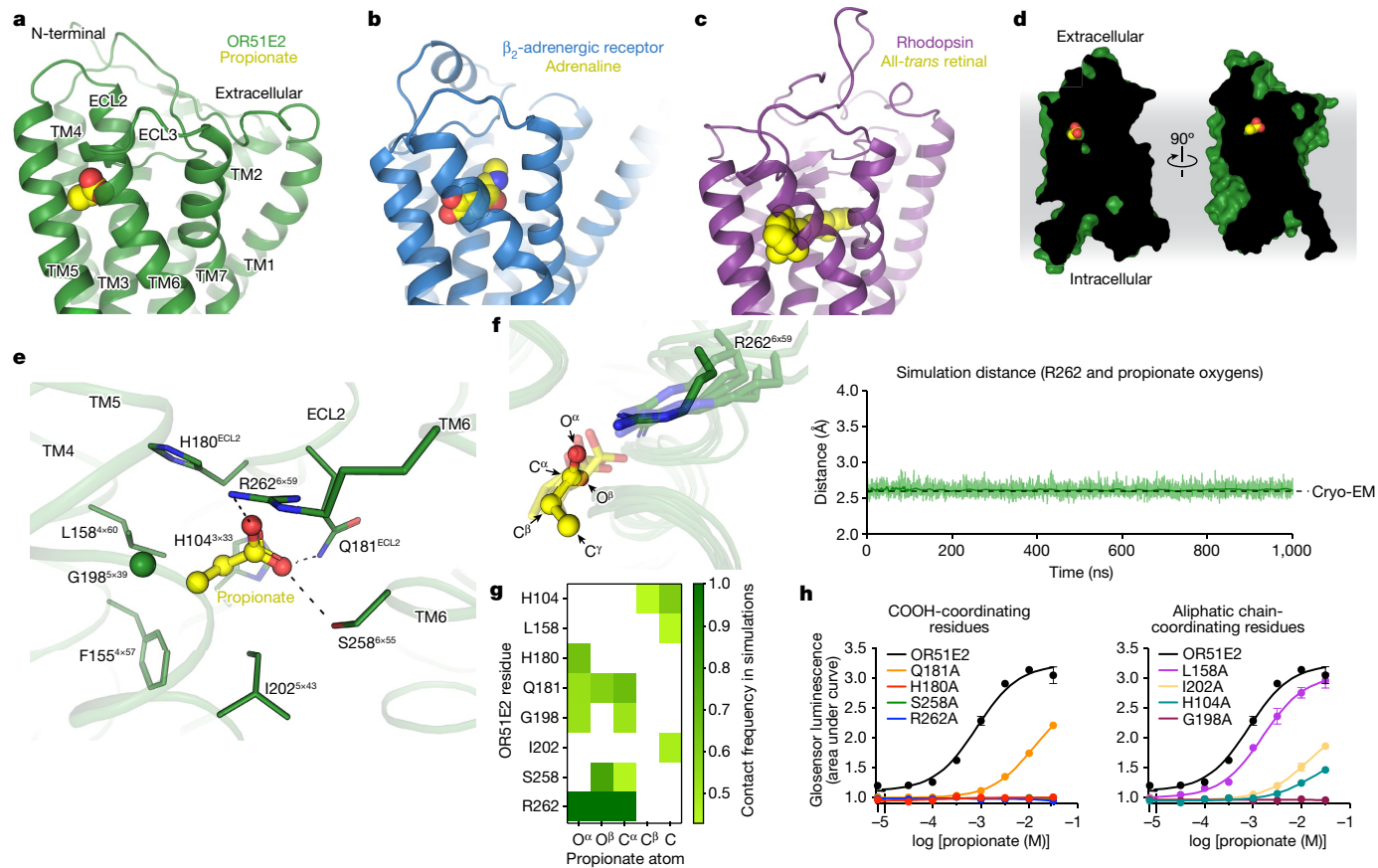


Fig. 2 | Odorant-binding pocket in OR51E2. **a–c**, Comparison of the propionate-binding site in OR51E2 (**a**) to two other prototypical class A GPCRs: β_2 AR bound to adrenaline (Protein Data Bank ID: 4LD0)³⁰ (**b**) and rhodopsin bound to all-trans retinal (Protein Data Bank ID: 6FUF)³¹ (**c**). Propionate primarily contacts TM4, TM5, TM6 and ECL2. By contrast, adrenaline and all-trans retinal make more extensive contacts with other GPCR transmembrane helices. **d**, The binding site of propionate in active OR51E2 is occluded from extracellular solvent. **e**, Close-up view of the propionate-binding site in OR51E2. **f**, Representative MD simulation snapshots of OR51E2 bound to propionate are shown as transparent sticks and overlaid on the cryo-EM structure (left). Displayed are the last snapshots of each simulation replicate, after 1,000 ns of simulation time. R262^{6x59} makes persistent contact with propionate over 1,000 ns of an individual simulation (see Extended Data Fig. 8 for data on other

simulation replicates; the complete MD simulation statistics are given in Supplementary Tables 1–6). The minimum distance between any of R262^{6x59} sidechain nitrogens and propionate oxygens is also shown (right). Green line indicates distance trajectory for a representative simulation. **g**, Heatmap of contact frequencies of interaction between OR51E2-binding site residues and propionate atoms (as labelled in **f**) obtained from five independent MD simulations each 1 μ s long (total time of 5 μ s). The contact frequency cut-off between receptor residue and ligand atoms was set at 40%. **h**, Alanine mutagenesis analysis of propionate-contacting residues (COOH-coordinating residues (left) and aliphatic chain-coordinating residues (right)) in OR51E2 using a real-time monitoring of the cAMP concentration assay. Small vertical line indicates intercept with y axis ($x=0$). Data points are mean \pm standard deviation from $n=3$ experiments.

an average distance that is identical to that observed in the cryo-EM structure (Fig. 2f and Extended Data Fig. 5). Simulations also supported persistent interactions between the propionate carboxylic group and S258^{6x55}, with additional contacting residues outlined in Fig. 2g. Indeed, alanine mutations for these carboxylic group-coordinating residues, with the exception of Q181^{4x53}, abolished propionate-induced activation of OR51E2 (Fig. 2h).

The van der Waals contacts between the propionate aliphatic group and OR51E2 are governed by tight packing interactions. The aliphatic portion of propionate contacts residues in TM3 (H104^{3x33}), TM4 (F155^{4x57} and L158^{4x60}) and TM5 (G198^{5x39} and I202^{5x43}). Unlike the persistent contacts observed for the oxygens in the carboxylic acid group, interactions between specific propionate carbon atoms and aliphatic residues in OR51E2 were more dynamic in simulations (Fig. 2g) and showed minimal contact with F155^{4x57}. However, alanine mutations to G198^{5x39}, I202^{5x43} and H104^{3x33} decreased propionate activity at OR51E2, suggesting that there are specific spatial requirements for propionate to bind to and activate the receptor. By contrast, propionate is only moderately less efficacious at OR51E2 with the L158^{4x60}A mutation (Fig. 2h), probably because this residue only engages the distal C γ carbon of

propionate. OR51E2 therefore recognizes propionate with specific ionic and hydrogen-bonding interactions combined with more distributed van der Waals interactions with tight shape complementarity.

Tuning OR selectivity

Many ORs are capable of responding to a wide diversity of chemically distinct odorants^{2,20}. By contrast, class I ORs are generally more restricted to carboxylic acid odorants³⁵. We tested the selectivity of OR51E2 for fatty acid odorants of various chain lengths to understand how structural features in the receptor lead to odorant specificity. Consistent with previous reports^{25,36}, we identified that acetate (C2) and propionate (C3) activate OR51E2 with millimolar potency (Fig. 3a,b). By contrast, longer chain length fatty acids (C4–C10) were either poorly or not active at OR51E2.

We speculated that the selectivity of OR51E2 for short-chain fatty acids arises from the restricted volume of the occluded binding pocket (31 Å³), which would accommodate short-chain fatty acids such as acetate and propionate but would preclude binding of fatty acids with longer aliphatic chain lengths (Fig. 3c). We therefore hypothesized that

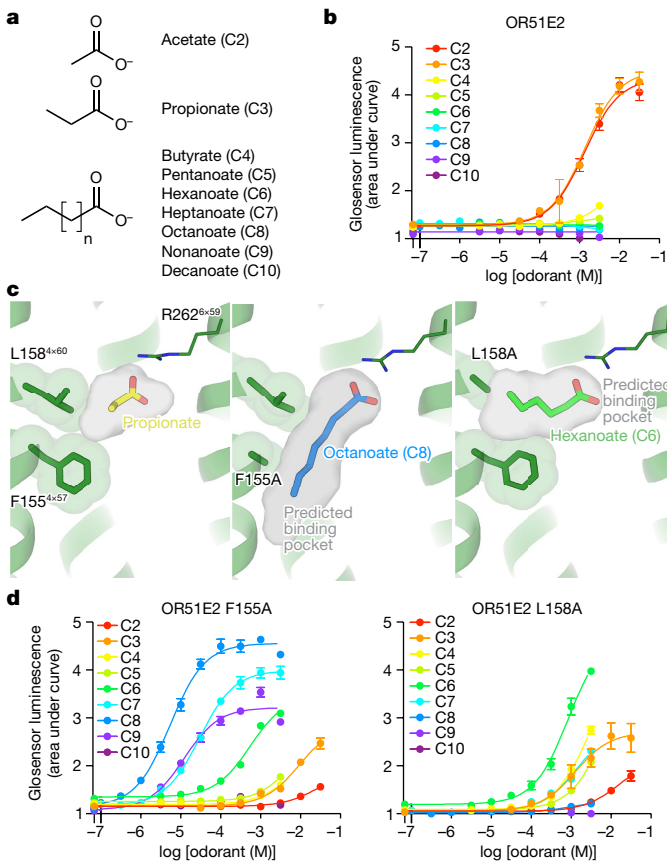


Fig. 3 | Tuning OR51E2 odorant selectivity. **a,b**, OR51E2 responds selectively to the short-chain fatty acids acetate and propionate as measured by a cAMP production assay. **c**, Docked poses of octanoate (C8) and hexanoate (C6) are shown in the predicted binding cavities of homology modelled OR51E2 mutants F155^{4×57}A and L158^{4×60}A. The binding pocket cavities are shown as a grey surface. Replacement of F155^{4×57} and L158^{4×60} with alanine is predicted to yield a binding pocket with increased volume capable of accommodating longer chain fatty acids. **d**, The F155^{4×57}A (left) and L158^{4×60}A (right) mutations in OR51E2 lead to increased sensitivity to long-chain fatty acids. Conversely, the potency for acetate and propionate is reduced for these two mutants. Small vertical lines (**b,d**) indicate intercept with y axis ($x=0$). Data points in **b** and **d** are mean \pm standard deviation from $n=4$ experiments.

the volume of the binding pocket acts as a selectivity determinant for fatty acid chain length. To directly test this hypothesis, we designed two mutations that are predicted to result in increased binding pocket volumes while maintaining the specific contacts with R262^{6×59} important for fatty acid activation of OR51E2. More specifically, we mutated two residues that are proximal to the carbon chain of propionate: F155^{4×57} and L158^{4×60}. Computational modelling of the F155^{4×57}A and L158^{4×60}A mutations predicted pocket volumes of 90 Å³ and 68 Å³, respectively, suggesting that both mutants should sufficiently accommodate fatty acids with longer chain length (Fig. 3c). Indeed, in cAMP assays, both the F155^{4×57}A and L158^{4×60}A OR51E2 mutants were broadly responsive to longer chain fatty acids (Fig. 3d and Extended Data Tables 2 and 3). The size of each binding pocket was correlated with the maximum chain length tolerated and, additionally, with the chain length that had the greatest potency. For example, F155^{4×57}A is responsive to a range of fatty acids (C2–C9), with octanoate (C8) displaying maximal potency and efficacy. By contrast, hexanoate (C6) is the most efficacious agonist at the L158^{4×60}A mutant. For both of these mutations, the potency of acetate and propionate is reduced compared with OR51E2, suggesting that tight packing interactions with the aliphatic chain is an important determinant of agonist potency.

We next examined the conservation of selectivity determining residues in both human class I and class II ORs. Reflecting its importance in carboxylic acid recognition, arginine is highly conserved in the 6×59 position in most human class I ORs (class I 71% versus class II 7%) (Extended Data Fig. 6). Positions 4×57 and 4×60 in all human class I ORs are constrained to aliphatic amino acids of different size (V/I/L/M/F, class I more than 80% versus class II less than 15%). By contrast, none of these positions has similar constraints in class II ORs. We surmise that the conserved residue R^{6×59} may anchor odorants in many class I OR binding pockets, whereas diversity in the 4×57, 4×60 and other binding pocket positions tune the binding pocket to enable selective recognition of the remainder of the molecule. Indeed, OR51L1 and OR51E1 contain substitutions at either 4×57, 4×60 or other binding pocket residues, which probably enables these receptors to respond to longer chain fatty acids²⁰. Two features may therefore drive odorant recognition for class I ORs: (1) hydrogen bonding or ionic interactions that anchor polar features of odorants to conserved OR binding pocket residues, and (2) van der Waals interactions of diverse aliphatic residues in the OR binding pocket that define a closed volume having a geometry that closely matches the shape of cognate odorants.

Activation mechanisms of OR51E2

Odorant binding to ORs is predicted to cause conformational changes in the receptor that enable engagement of G proteins. Our strategy to stabilize OR51E2 with miniG_s precluded structure determination of inactive OR51E2 in the absence of an odorant. We therefore turned to comparative structural modelling, mutagenesis studies and MD simulations to understand the effect of propionate binding on the conformation of OR51E2.

Comparison of active OR51E2 to G_s-coupled, active-state β₂AR demonstrated that both receptors engage the G protein with a similar overall orientation of the 7TM domain and Gα_s (Fig. 4a and Extended Data Fig. 7). A central hallmark of class A GPCR activation is an outward displacement and rotation of TM6 in the cytoplasmic side of the receptor, which is accompanied by more subtle movement of the other TM helices^{37–39}. These conformational changes create a cavity for the G protein C-terminal α-helix. Previous structural biology studies have identified two regions conserved in class A GPCRs that are critically important for allosteric communication between the agonist-binding site and the G protein-binding site: a connector region that is adjacent to the ligand-binding site and a G protein-coupling region adjacent to the Gα_s C-terminal α-helix³⁷ (Fig. 4a). We aimed to understand how propionate binding to OR51E2 stabilizes these regions in an active conformation. Although the overall conformation of OR51E2 and β₂AR is similar (root-mean-square deviation of 3.1 Å over all resolved Cα atoms; see Supplementary Table 8), the specific sequences that define the G protein-coupling and connector regions are distinct between ORs and non-olfactory class A GPCRs. Comparison of sequence conservation in TM6 between human ORs and non-olfactory class A GPCRs revealed a highly conserved motif (KAFSTCxSH^{6×40}) in the G protein-coupling region in ORs that is absent in non-ORs (Fig. 4b). By contrast, the highly conserved CWxP^{6×50} motif in the connector region of class A GPCRs is absent in ORs. Instead, ORs contain the previously described FYGx^{6×50} motif in the connector region⁴⁰ (Fig. 4f,g).

Closer inspection of the G protein-coupling region in OR51E2 revealed a unique hydrogen-bonding network between the highly conserved residues R121^{3×50} in TM3, H243^{6×40} in TM6 and Y217^{5×58} in TM5 that is not observed in other class A GPCRs (Fig. 4c,d). Activation of the β₂AR is associated with an inward movement of TM7 that positions Y316^{7×53} within a water-mediated hydrogen-bonding distance of Y219^{5×58}; this movement leads to outward movement of TM6 by displacing the aliphatic I278^{6×40} residue (Fig. 4d). Given the high conservation of R^{3×50}, H^{6×40} and Y^{5×58} across all ORs (89%, 97% and 93%, respectively; Extended Data Fig. 7), we propose that this contact is important in stabilizing

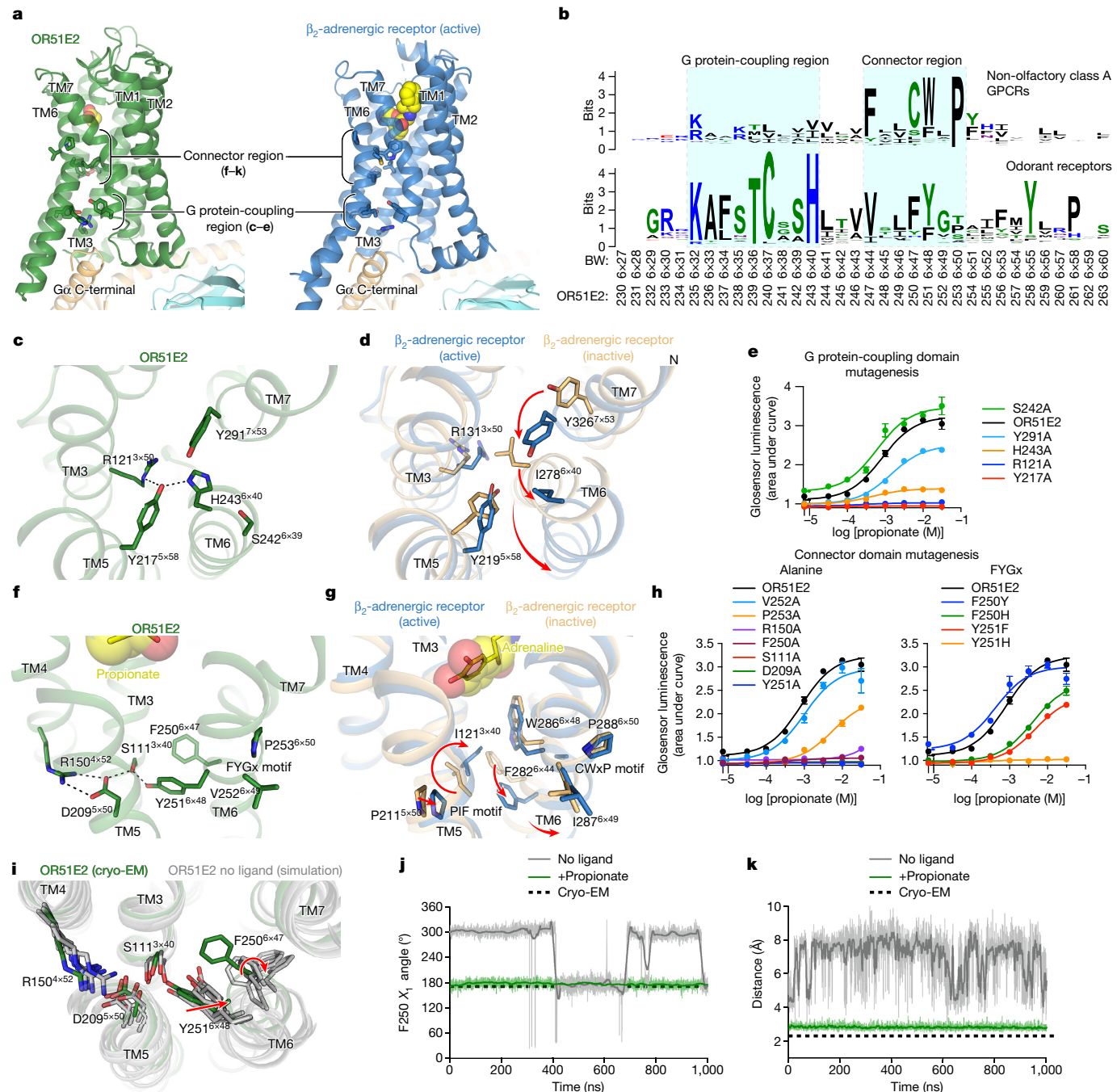


Fig. 4 | Activation mechanism of OR51E2. **a**, Ribbon diagram comparing structures of the propionate-bound OR51E2–miniG_s complex (propionate shown as spheres within green ribbon) to the BI-167107-bound β₂AR–G_s complex (Protein Data Bank ID: 3SN6; BI-167107 shown as spheres within blue ribbon). For both receptors, the connector region couples conformational changes at the ligand-binding site with the G protein-coupling region. **b**, Weblogo depicting conservation of TM6 in either human ORs or human non-olfactory class A GPCRs. Amino acid numbering for OR51E2 and Ballosters–Weinstein (BW) are indicated. **c,d**, Close-up view of the G protein-coupling domain in active OR51E2 (**c**) and both active and inactive β₂AR (**d**). Activation of β₂AR is associated with an inward movement of TM7 and a contact between Y219^{5x58} and Y326^{7x53}. In OR51E2, H243^{6x40} interacts with Y217^{5x58} in the active state. **e**, Alanine mutagenesis of G protein-coupling domain residues in OR51E2 using a real-time cAMP concentration assay. **f,g**, Close-up views of the connector region in active OR51E2 (**f**) and both active and inactive β₂AR (**g**). **h**, Mutagenesis of connector region residues (alanine (left) and FYGx (right)) in OR51E2 using a real-time cAMP concentration assay. **i**, MD simulations of

OR51E2 with propionate removed. Snapshots displayed are the last snapshot from each of the five independent simulation replicates after 1,000 ns of simulation time. Simulations show increased flexibility of TM6 in the connector region residues. Snapshots extracted from unbiased clustering analysis of the entire ensemble of MD trajectories show similar structural changes as these last snapshots (see Methods; Supplementary Table 7 and Supplementary Fig. 1). **j,k**, MD trajectories for a representative simulation showing rotation of sidechain rotamer angle of F250^{6x47} (**j**) and minimum distance between S111^{3x40} and Y251^{6x48} hydroxyl groups (**k**) performed with or without propionate over the course of 1,000-ns MD simulations (see Extended Data Fig. 8 for simulation replicates). The thick traces represent smoothed values with an averaging window of 8 ns; the thin traces represent unsmoothed values. Data points in **e** and **h** are mean ± standard deviation from $n = 4$ experiments. Small vertical lines (**e,h**) indicate intercept with y axis ($x = 0$). Dashed lines in **c** and **f** represent hydrogen bonds. Red arrows in **d** and **g** indicate movements between inactive and active β₂AR. In **i**, red arrows indicate conformational changes in OR51E2 seen in simulations.

the active conformation of the OR. Indeed, alanine mutagenesis of OR51E2 residues in the G protein-coupling region show a dramatic loss of activity for H243^{6×40}, Y217^{5×58} and R121^{3×50} mutants associated with poor receptor expression (Fig. 4e and Extended Data Table 2). By contrast, mutation of Y291^{7×53} in OR51E2 has a more modest effect on propionate activity.

We next examined the connector region of OR51E2 directly adjacent to the propionate-binding site (Fig. 4f). Activation of the β_2 AR is associated with a rearrangement of the PIF motif between positions I^{3×40} (TM3), P^{5×50} (TM5) and F^{6×44} (TM6), which leads to an outward displacement of TM6 at the intracellular side. This coordinated movement has been shown in the majority of class A GPCRs by comparative analysis of available active-state and inactive-state structures^{37–39}. Conservation at the PIF positions is low in ORs, suggesting an alternative mechanism. In OR51E2, we observed an extended hydrogen-bonding network between Y251^{6×48} of the OR-specific FYGx motif and residues in TM3 (S111^{3×40}), TM4 (R150^{4×52}) and TM5 (D209^{5×50}). Of note, the intramembrane ionic interaction between D209^{5×50} and R150^{4×52} is only conserved in class I ORs (class I: D^{5×50} is 82% and R^{4×52} is 88%; class II: D^{5×50} is 0.3% and R^{4×52} is 0%; Extended Data Fig. 7). Alanine mutagenesis of most residues in this connector region of OR51E2 abolishes response to propionate (Fig. 4h), in part because mutations in this region dramatically decrease receptor expression (Extended Data Table 2). More conservative substitutions to F250^{6×47} or Y251^{6×48} also show impairment in OR51E2 function, suggesting that the specific contacts observed in active OR51E2 are important for robust receptor activation.

We turned to MD simulations to examine how ligand binding influences the conformation of the connector region. After removing the G protein, we simulated OR51E2 with and without propionate in the binding site. For each condition, we performed five 1- μ s simulations. OR51E2 simulated with propionate remains in a conformation similar to the cryo-EM structure. In the absence of propionate, the connector region of OR51E2 displays more flexibility in simulations (Fig. 4i and Extended Data Fig. 8). In both of these conditions, we did not observe deactivation of OR51E2, probably because this transition requires greater than 1 μ s of simulation time⁴¹. We observed two motions in the FYGx motif associated with this increased conformational heterogeneity: a rotameric flexibility of F250^{6×47} between the experimentally observed conformation and alternative rotamers, and a disruption of a hydrogen bond between Y251^{6×48} and S111^{3×40} (Fig. 4j,k and Extended Data Fig. 8). Simulations without propionate show that the distance between the hydroxyl groups of Y251^{6×48} and S111^{3×40} is more than 4 Å, indicating the loss of a hydrogen bond that was observed in both the cryo-EM structure of OR51E2 and the MD simulations with propionate (Fig. 4k and Extended Data Fig. 8). On the basis of structural comparison to other class A GPCRs, mutagenesis studies and MD simulations, we therefore propose that odorant binding stabilizes the conformation of an otherwise dynamic FYGx motif to drive OR activation.

Structural dynamics of ECL3 in OR function

ORs display substantial sequence variation in ECL3, a region previously shown to be critical for recognition of highly diverse odorants^{42,43}. We therefore aimed to understand the involvement of ECL3 in propionate binding to OR51E2 and, more generally, how ECL3 may drive the conformational changes in TM6 necessary for activation of the OR (Fig. 5). In our structure of OR51E2, ECL3 is directly coupled to odorant binding via a direct interaction between the carboxylic acid moiety of propionate and the ECL3 adjacent residue R262^{6×59} (Fig. 5a). To investigate the role of R262^{6×59} in maintaining the conformation of ECL3 by binding the odorant, we analysed simulations of OR51E2 performed without propionate. In the absence of coordination with the carboxylic acid group of propionate, R262^{6×59} showed a marked increase in flexibility, with an outward movement of up to 8 Å away from the ligand-binding

site (Fig. 5b,c). This movement is accompanied by displacement of ECL3 away from the odorant-binding pocket.

To test whether inward movement of R262^{6×59} is itself sufficient to activate OR51E2, we designed a gain-of-function experiment. We hypothesized that introduction of an acidic residue in the binding pocket with an appropriate geometry may substitute for the carboxylic acid of propionate and coordinate R262^{6×59}. Indeed, substitution of Asp in position 45⁵³ (Q181^{45×53}D) of OR51E2 yielded increased basal activity of cAMP (Fig. 5d). By contrast, introduction of Glu in the same position (Q181^{45×53}E) rendered OR51E2 largely inactive, suggesting the requirement for a precise coordination geometry for R262^{6×59}. Substitution with the larger Gln (Q181^{45×53}N) rendered OR51E2 completely unresponsive to propionate, either by sterically blocking R262^{6×59} or by displacing propionate itself. In simulations of OR51E2 with the Q181^{45×53}D substitution, R262^{6×59} is persistently engaged towards the ligand-binding site (Fig. 5b). Furthermore, this inward movement of R262^{6×59} and ECL3 is accompanied by activation-associated conformational changes in the connector domain of OR51E2 (Extended Data Fig. 9), perhaps explaining the basal activity of the Q181^{45×53}D mutant. Inward movement of ECL3 is therefore sufficient to activate OR51E2.

Because conformational changes in ECL3 are critical to OR51E2 activation, we speculated that this region may provide a common activation mechanism across the OR family. To probe this notion, we examined structural predictions of all human ORs by AlphaFold2 (ref.⁴⁴). We first compared the AlphaFold2 prediction for OR51E2 with the cryo-EM structure, which yielded a high degree of agreement reflected in a root-mean-square deviation of 1.3 Å for C α atoms. The AlphaFold2-predicted structure of OR51E2 appears to be in an intermediate or inactive conformation characterized by outward displacement of R262^{6×59} and ECL3, a G protein-coupling domain in the inactive conformation, and TM6 more inwardly posed than active OR51E2 (Fig 5e and Extended Data Fig. 10). We next examined the predicted structures of all human ORs, which revealed a largely shared topology for the extracellular region for the broader family (Fig. 5f). Indeed, the per-residue confidence score from AlphaFold2 (predicted local distance difference test) for the N terminus, ECL1 and ECL2 are predicted with high confidence for most ORs. By contrast, ECL3 shows lower predicted local distance difference test scores. Because low predicted local distance difference test scores correlate with disordered protein regions⁴⁴, we surmise that, in the absence of odorant binding, the structure of ECL3 is less constrained than the rest of the odorant-binding pocket for the broader OR family. Similar to OR51E2, odorant binding may therefore stabilize ECL3 to drive receptor activation for the broader OR family.

Discussion

We propose the following model for activation of OR51E2 (Fig. 5g). In the unbound state, the extracellular segment of TM6 is dynamic. After binding of propionate, TM6 rotates inward towards the 7TM domain and is stabilized via a direct coordination of the propionate carboxylic acid via R262^{6×59}. The conserved FYGx motif in TM6 acts as a structural pivot point around which TM6 rotates to displace the intracellular end of TM6 from the TM core and open the canonical active G protein-binding site. Although specific interactions between the propionate aliphatic chain and residues within the binding site are important for achieving full potency of the odorant response, OR51E2 is constitutively active when an aspartate residue (Q181^{45×53}D) is introduced in the binding pocket. This suggests that the observed rotation of TM6 mediated by coordination of R262^{6×59} with a stable anionic group in the binding site, in itself is sufficient for receptor activation. Although this model remains speculative owing to the lack of an experimentally determined inactive-state structure of OR51E2, it integrates the findings from unique structural features of ORs compared with other class A GPCRs, MD simulations and mutagenesis studies. A similar mechanism may be responsible for the activation of most class I ORs, a large

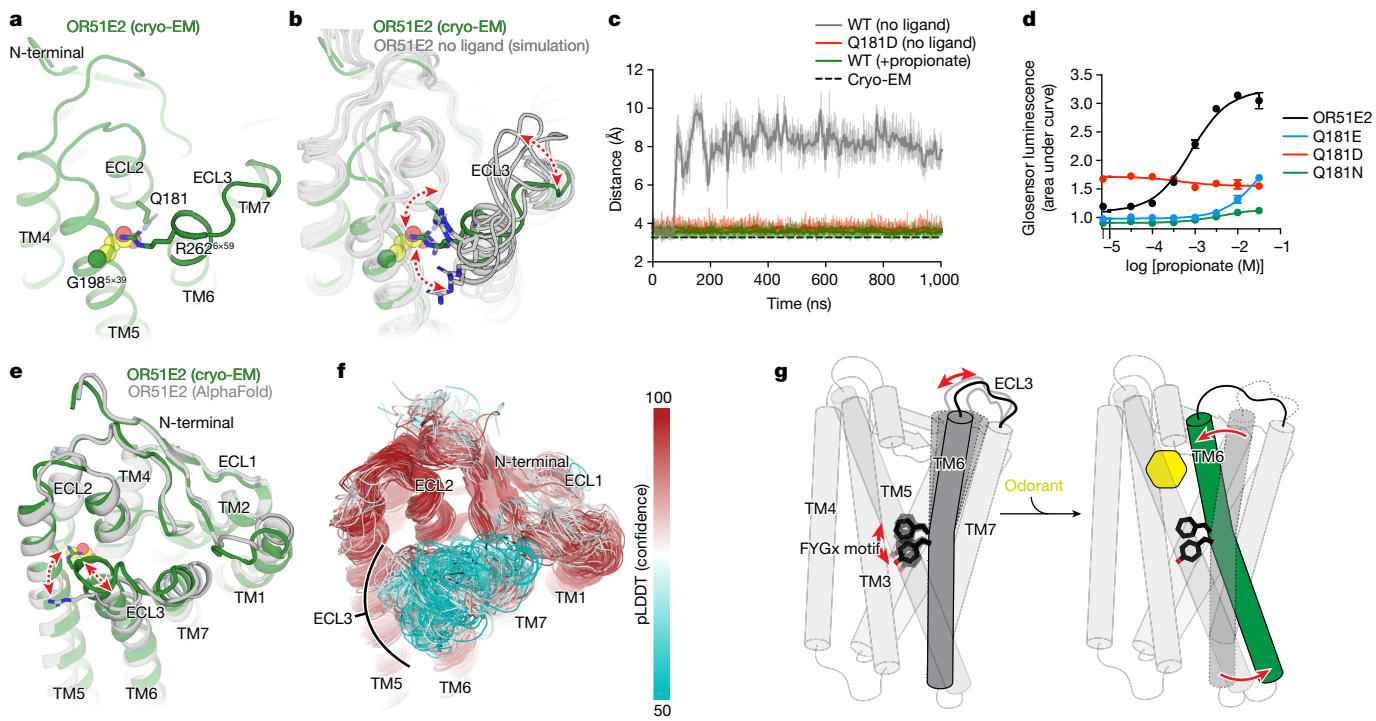


Fig. 5 | Structural dynamics of ECL3 in OR function. **a**, Residue R262^{6×59} in ECL3 makes critical contact with propionate. Residue Q181^{45×53} in ECL2 is highlighted. **b**, MD simulations of OR51E2 with propionate removed show increased flexibility of R262^{6×59}. Representative snapshots are displayed from five independent simulation replicates after 1,000 ns of simulation time. Red arrows indicate conformational flexibility observed in simulations. **c**, In simulations of wild-type (WT) OR51E2 bound to propionate, the minimum distance between R262^{6×59} and G198^{5×39} heavy atoms is stable and similar to the cryo-EM structure. Simulations of WT OR51E2 without propionate (no ligand) show increased minimum distance between R262^{6×59} and G198^{5×39}. In simulations of the Q181^{45×53}D mutant without propionate, the minimum distance between R262^{6×59} and G198^{5×39} is similar to WT OR51E2 bound to propionate. Minimum distance was measured between R262^{6×59} sidechain atoms and G198^{5×39} main chain atoms (excluding the hydrogens) over the course of 1,000 ns MD simulations (see Extended Data Fig. 8 for simulation replicates).

The thick traces represent smoothed values with an averaging window of 8 ns; the thin traces represent unsmoothed values. **d**, Conservative mutagenesis of Q181^{45×53} shows that the Q181^{45×53}D mutant is constitutively active, potentially because it substitutes a carboxylic acid in the OR51E2-binding pocket. Small vertical line indicates intercept with y axis ($x=0$). **e**, Comparison of the cryo-EM structure of OR51E2 with the AlphaFold2-predicted structure shows high similarity in the extracellular domain with the exception of the ECL3 region. The AlphaFold2 model shows an outward displacement of R262^{6×59} and ECL3 similar to simulations of apo OR51E2. Red arrows indicate conformational differences between cryo-EM structure and AlphaFold2 prediction. **f**, AlphaFold2 predictions for all human ORs show low confidence in the ECL3 region and high confidence in other extracellular loops. pLDDT, predicted local distance difference test. **g**, A model for ECL3 as a key site for OR activation. Red arrows indicate movements required for OR51E2 activation.

majority of which recognize carboxylic acids and contain an arginine at position 6×59. The mechanism of activation of class II ORs, which recognize a broader range of volatile odorants and lack R^{6×59}, could be potentially distinct.

Our work illuminates the molecular underpinnings of odorant recognition in a vertebrate class I OR. Although the full breadth of potential odorants that activate OR51E2 remains to be characterized, profiling of known fatty acid odorants suggests that OR51E2 is narrowly tuned to short-chain fatty acids^{20,25}. Propionate binds to OR51E2 with two types of interactions: specific ionic and hydrogen-bonding interactions that anchor the carboxylic acid, and more nonspecific hydrophobic contacts that rely on shape complementarity with the aliphatic portion of the ligand. We demonstrate that the specific geometric constraints imposed by the occluded OR51E2 odorant-binding pocket are responsible, in part, for this selectivity. Molecular recognition in OR51E2 is therefore distinct from the distributed hydrophobic interactions that mediate odorant recognition at an insect odorant-gated ion channel¹². We anticipate that the molecular mechanism that we define here for OR51E2 is likely to extend to other class I ORs that recognize polar, water-soluble odorants with multiple hydrogen bond acceptors and donors. Molecular recognition by more broadly tuned ORs, and the larger class II OR family, however, remains to be defined.

The structural basis of ligand recognition for OR51E2 also provides insight into evolution of the OR family. Unlike most vertebrate OR genes that have evolved rapidly via gene duplication and diversification, OR51E2 is one of a few ORs with strong evolutionary conservation within different species⁵. This constraint may result from recognition of odorants important for survival or from vital non-olfactory roles of OR51E2 activity detecting propionate and acetate, the main metabolites produced by the gut microbiota. Molecular recognition of propionate by OR51E2 may therefore represent a unique example of specificity within the broader OR family. Although future work will continue to decipher how hundreds of ORs sense an immensely large diversity of odorants, our structure and mechanistic insights into the function of OR51E2 provide a new foundation to understand our sense of smell at an atomic level.

Online content

Any methods, additional references, Nature Portfolio reporting summaries, source data, extended data, supplementary information, acknowledgements, peer review information; details of author contributions and competing interests; and statements of data and code availability are available at <https://doi.org/10.1038/s41586-023-05798-y>.

- Buck, L. & Axel, R. A novel multigene family may encode odorant receptors: a molecular basis for odor recognition. *Cell* **65**, 175–187 (1991).
- Malnic, B., Hirono, J., Sato, T. & Buck, L. B. Combinatorial receptor codes for odors. *Cell* **96**, 713–723 (1999).
- Zhao, H. et al. Functional expression of a mammalian odorant receptor. *Science* **279**, 237–242 (1998).
- Mayhew, E. J. et al. Transport features predict if a molecule is odorous. *Proc. Natl Acad. Sci. USA* **119**, e2116576119 (2022).
- Niimura, Y., Matsui, A. & Touhara, K. Extreme expansion of the olfactory receptor gene repertoire in African elephants and evolutionary dynamics of orthologous gene groups in 13 placental mammals. *Genome Res.* **24**, 1485–1496 (2014).
- Malnic, B., Godfrey, P. A. & Buck, L. B. The human olfactory receptor gene family. *Proc. Natl Acad. Sci. USA* **101**, 2584–2589 (2004).
- Bjarnadóttir, T. K. et al. Comprehensive repertoire and phylogenetic analysis of the G protein-coupled receptors in human and mouse. *Genomics* **88**, 263–273 (2006).
- Glusman, G., Yanai, I., Rubin, I. & Lancet, D. The complete human olfactory subgenome. *Genome Res.* **11**, 685–702 (2001).
- Jones, D. T. & Reed, R. R. GOLF: an olfactory neuron specific-G protein involved in odorant signal transduction. *Science* **244**, 790–795 (1989).
- Pourmrady, A. & Lomvardas, S. Olfactory receptor choice: a case study for gene regulation in a multi-enhancer system. *Curr. Opin. Genet. Dev.* **72**, 101–109 (2022).
- Butterwick, J. A. et al. Cryo-EM structure of the insect olfactory receptor Orco. *Nature* **560**, 447–452 (2018).
- Del Mármol, J., Yedlin, M. A. & Ruta, V. The structural basis of odorant recognition in insect olfactory receptors. *Nature* **597**, 126–131 (2021).
- Ikegami, K. et al. Structural instability and divergence from conserved residues underlie intracellular retention of mammalian odorant receptors. *Proc. Natl Acad. Sci. USA* **117**, 2957–2967 (2020).
- Saito, H., Kubota, M., Roberts, R. W., Chi, Q. & Matsunami, H. RTP family members induce functional expression of mammalian odorant receptors. *Cell* **119**, 679–691 (2004).
- Cook, B. L. et al. Large-scale production and study of a synthetic G protein-coupled receptor: human olfactory receptor 17-4. *Proc. Natl Acad. Sci. USA* **106**, 11925–11930 (2009).
- Katada, S., Tanaka, M. & Touhara, K. Structural determinants for membrane trafficking and G protein selectivity of a mouse olfactory receptor. *J. Neurochem.* **90**, 1453–1463 (2004).
- Lee, S. J., Depoortere, I. & Hatt, H. Therapeutic potential of ectopic olfactory and taste receptors. *Nat. Rev. Drug Discov.* **18**, 116–138 (2019).
- Freitag, J., Ludwig, G., Andreini, I., Rössler, P. & Breer, H. Olfactory receptors in aquatic and terrestrial vertebrates. *J. Comp. Physiol. A* **183**, 635–650 (1998).
- Shaya, H. J. et al. ER stress transforms random olfactory receptor choice into axon targeting precision. *Cell* **185**, 3896–3912.e22 (2022).
- Saito, H., Chi, Q., Zhuang, H., Matsunami, H. & Mainland, J. D. Odor coding by a mammalian receptor repertoire. *Sci. Signal.* **2**, ra9 (2009).
- Xu, L. L. et al. PSGR, a novel prostate-specific gene with homology to a G protein-coupled receptor, is overexpressed in prostate cancer. *Cancer Res.* **60**, 6568–6572 (2000).
- Gelis, L. et al. Functional characterization of the odorant receptor 51E2 in human melanocytes. *J. Biol. Chem.* **291**, 17772–17786 (2016).
- Kotto, K. et al. The olfactory G protein-coupled receptor (Olfr-78/OR51E2) modulates the intestinal response to colitis. *Am. J. Physiol. Cell Physiol.* **318**, C502–C513 (2020).
- Vadevo, S. M. P. et al. The macrophage odorant receptor Olfr78 mediates the lactate-induced M2 phenotype of tumor-associated macrophages. *Proc. Natl Acad. Sci. USA* **118**, e2102434118 (2021).
- Pluznick, J. L. et al. Olfactory receptor responding to gut microbiota-derived signals plays a role in renin secretion and blood pressure regulation. *Proc. Natl Acad. Sci. USA* **110**, 4410–4415 (2013).
- Flegel, C., Manteniotis, S., Osthold, S., Hatt, H. & Gisselmann, G. Expression profile of ectopic olfactory receptors determined by deep sequencing. *PLoS ONE* **8**, e55368 (2013).
- Nakashima, A. et al. Agonist-independent GPCR activity regulates anterior–posterior targeting of olfactory sensory neurons. *Cell* **154**, 1314–1325 (2013).
- Rasmussen, S. G. F. et al. Crystal structure of the β_2 -adrenergic receptor–G_s protein complex. *Nature* **477**, 549–555 (2011).
- Nehmé, R. et al. Mini-G proteins: novel tools for studying GPCRs in their active conformation. *PLoS ONE* **12**, e0175642 (2017).
- Ring, A. M. et al. Adrenaline-activated structure of β_2 -adrenoceptor stabilized by an engineered nanobody. *Nature* **502**, 575–579 (2013).
- Tsai, C. J. et al. Crystal structure of rhodopsin in complex with a mini-G_s sheds light on the principles of G protein selectivity. *Sci. Adv.* **4**, eaat7052 (2018).
- Ballesteros, J. A. & Weinstein, H. [19] Integrated methods for the construction of three-dimensional models and computational probing of structure–function relations in G protein-coupled receptors. *Methods Neurosci.* **25**, 366–428 (1995).
- de March, C. A., Kim, S. K., Antonczak, S., Goddard, W. A. 3rd & Golebiowski, J. G protein-coupled odorant receptors: from sequence to structure. *Protein Sci.* **24**, 1543–1548 (2015).
- Isberg, V. et al. Generic GPCR residue numbers—aligning topology maps while minding the gaps. *Trends Pharmacol. Sci.* **36**, 22–31 (2015).
- Cichy, A., Shah, A., Dewan, A., Kaye, S. & Bozza, T. Genetic depletion of class I odorant receptors impacts perception of carboxylic acids. *Curr. Biol.* **29**, 2687–2697.e4 (2019).
- Pronin, A. & Slepak, V. Ectopically expressed olfactory receptors OR51E1 and OR51E2 suppress proliferation and promote cell death in a prostate cancer cell line. *J. Biol. Chem.* **296**, 100475 (2021).
- Manglik, A. & Kruse, A. C. Structural basis for G protein-coupled receptor activation. *Biochemistry* **56**, 5628–5634 (2017).
- Zhou, Q. et al. Common activation mechanism of class A GPCRs. *eLife* **8**, e50279 (2019).
- Hauser, A. S. et al. GPCR activation mechanisms across classes and macro/microscales. *Nat. Struct. Mol. Biol.* **28**, 879–888 (2021).
- de March, C. A. et al. Conserved residues control activation of mammalian G protein-coupled odorant receptors. *J. Am. Chem. Soc.* **137**, 8611–8616 (2015).
- Dror, R. O. et al. Activation mechanism of the β_2 -adrenergic receptor. *Proc. Natl Acad. Sci. USA* **108**, 18684–18689 (2011).
- Bushdid, C. et al. Mammalian class I odorant receptors exhibit a conserved vestibular-binding pocket. *Cell. Mol. Life Sci.* **76**, 995–1004 (2019).
- Shim, T. et al. The third extracellular loop of mammalian odorant receptors is involved in ligand binding. *Int. J. Mol. Sci.* **23**, 12501 (2022).
- Jumper, J. et al. Highly accurate protein structure prediction with AlphaFold. *Nature* **596**, 583–589 (2021).

Publisher's note Springer Nature remains neutral with regard to jurisdictional claims in published maps and institutional affiliations.

Springer Nature or its licensor (e.g. a society or other partner) holds exclusive rights to this article under a publishing agreement with the author(s) or other rightsholder(s); author self-archiving of the accepted manuscript version of this article is solely governed by the terms of such publishing agreement and applicable law.

© The Author(s), under exclusive licence to Springer Nature Limited 2023

Methods

Expression and purification of OR51E2–miniG_s protein

Human *OR51E2* (Uniprot: Q9H255) was cloned into pCDNA-Zeo-TetO, a custom pcDNA3.1 vector containing a tetracycline-inducible gene expression cassette⁴⁵. The construct included an N-terminal influenza haemagglutinin signal sequence and the FLAG (DYKDDDK) epitope tag. The construct further included the miniG_{s399} protein⁵, which was fused to the C terminus of OR51E2 with a human rhinovirus 3C (HRV 3C) protease cleavage sequence flanked by Gly–Ser linkers.

The resulting construct (OR51E2–miniG_{s399}) was transfected into 11 of inducible Expi293F-TetR cells (unauthenticated and untested for mycoplasma contamination; Thermo Fisher) using the ExpiFectamine 293 Transfection Kit (Thermo Fisher) as per the manufacturer's instructions. After 16 h, protein expression was induced with 1 µg ml⁻¹ doxycycline hydyclate (Sigma Aldrich), and the culture was placed in a shaking incubator maintained at 37 °C and a 5% CO₂ atmosphere. After 36 h, cells were harvested by centrifugation and stored at –80 °C.

For receptor purification, cells were thawed and hypotonically lysed in 50 mM HEPES, pH 7.5, 1 mM EDTA, 30 mM sodium propionate (Sigma Aldrich), 100 µM tris(2-carboxyethyl)phosphine (TCEP; Fischer Scientific), 160 µg ml⁻¹ benzamidine and 2 µg ml⁻¹ leupeptin for 15 min at 4 °C. Lysed cells were harvested by centrifugation at 16,000g for 15 min and immediately dounce-homogenized in ice-cold solubilization buffer comprising 50 mM HEPES, pH 7.5, 300 mM NaCl, 1% (w/v) lauryl maltose neopentyl glycol (L-MNG; Anatrace), 0.1% (w/v) cholestryl hemisuccinate (CHS, Steraloids), 30 mM sodium propionate, 5 mM adenosine 5'-triphosphate (ATP; Fischer Scientific), 2 mM MgCl₂, 100 µM TCEP, 160 µg ml⁻¹ benzamidine and 2 µg ml⁻¹ leupeptin. The sample was stirred for 2 h at 4 °C, and the detergent-solubilized fraction was clarified by centrifugation at 20,000g for 30 min. The detergent-solubilized sample was supplemented with 4 mM CaCl₂ and incubated in batch with homemade M1-FLAG antibody conjugated CNBr-Sepharose under slow rotation for 1.5 h at 4 °C. The Sepharose resin was transferred to a glass column and washed with 20 column volumes of ice-cold buffer comprising 50 mM HEPES, pH 7.5, 300 mM NaCl, 0.05% (w/v) L-MNG, 0.005% (w/v) CHS, 30 mM sodium propionate, 2.5 mM ATP, 4 mM CaCl₂, 2 mM MgCl₂ and 100 µM TCEP. This was followed by 10 column volumes of ice-cold 50 mM HEPES, pH 7.5, 150 mM NaCl, 0.0075% (w/v) L-MNG, 0.0025% glyco-diosgenin (GDN; Anatrace), 0.001% (w/v) CHS, 30 mM sodium propionate, 4 mM CaCl₂ and 100 µM TCEP. Receptor-containing fractions were eluted with ice-cold 50 mM HEPES, pH 7.5, 150 mM NaCl, 0.0075% (w/v) L-MNG, 0.0025% (w/v) GDN, 0.001% (w/v) CHS, 30 mM sodium propionate, 5 mM EDTA, 100 µM TCEP and 0.2 mg ml⁻¹ FLAG peptide. Fractions containing the OR51E2–miniG_{s399} fusion protein were concentrated in a 50-kDa MWCO spin filter (Amicon) and further purified over a Superdex 200 Increase 10/300 GL (Cytiva) size-exclusion chromatography (SEC) column, which was equilibrated with 20 mM HEPES, pH 7.5, 150 mM NaCl, 0.005% (w/v) GDN, 0.0005% CHS, 30 mM sodium propionate and 100 µM TCEP. Fractions containing monodisperse OR51E2–miniG_{s399} were combined and concentrated in a 50-kDa MWCO spin filter before complexing with Gβ₁γ₂ and Nb35.

Expression and purification of Gβ₁γ₂

A baculovirus was generated with the pVLDual expression vector encoding both the human Gβ₁ subunit with a HRV 3C cleavable N-terminal 6× His-tag and the untagged human Gγ₂ subunit, in *Spodoptera frugiperda* SF9 insect cells (unauthenticated and untested for mycoplasma contamination; Expression Systems). For expression, *Trichoplusia ni* Hi5 insect cells (unauthenticated and untested for mycoplasma contamination; Expression Systems) were infected at a density of 3.0 × 10⁶ cells per ml with high titre Gβ₁γ₂-baculovirus, and grown at 27 °C with 130 r.p.m. shaking. After 48 h, cells were harvested and resuspended in lysis buffer comprising 20 mM HEPES, pH 8, 5 mM β-mercaptoethanol (β-ME), 20 µg ml⁻¹ leupeptin and 160 µg ml⁻¹ benzamidine. Lysed cells were

pelleted at 20,000g for 15 min, and solubilized with 20 mM HEPES, pH 8, 100 mM sodium chloride, 1% (w/v) sodium cholate (Sigma Aldrich), 0.05% (w/v) n-dodecyl-β-D-maltopyranoside (DM; Anatrace) and 5 mM β-ME. Solubilized Gβ₁γ₂ was clarified by centrifugation at 20,000g for 30 min and was then incubated in batch with HisPur Ni-NTA resin (Thermo Scientific). Resin-bound Gβ₁γ₂ was washed extensively, before detergent was slowly exchanged on-column to 0.1% (w/v) L-MNG and 0.01% (w/v) CHS. Gβ₁γ₂ was eluted with 20 mM HEPES pH 7.5, 100 mM NaCl, 0.1% (w/v) L-MNG, 0.01% (w/v) CHS, 300 mM imidazole, 1 mM DL-dithiothreitol (DTT), 20 µg ml⁻¹ leupeptin and 160 µg ml⁻¹ benzamidine. Fractions containing Gβ₁γ₂ were pooled and supplemented with homemade 3C protease before overnight dialysis into buffer comprising 20 mM HEPES, pH 7.5, 100 mM NaCl, 0.02% (w/v) L-MNG, 0.002% (w/v) CHS, 1 mM DTT and 10 mM imidazole. Uncleaved Gβ₁γ₂ was removed by batch incubation with Ni-NTA resin, before the unbound fraction containing cleaved Gβ₁γ₂ was dephosphorylated by treatment with lambda phosphatase (New England Biolabs), calf intestinal phosphatase (New England Biolabs) and antarctic phosphatase (New England Biolabs) for 1 h at 4 °C. The geranylgeranylated Gβ₁γ₂ heterodimer was isolated by anion exchange chromatography using a MonoQ 4.6/100 PE (Cytiva) column, before overnight dialysis in 20 mM HEPES, pH 7.5, 100 mM NaCl, 0.02% (w/v) L-MNG and 100 µM TCEP. The final sample was concentrated on a 3-kDa MWCO spin filter (Amicon), and 20% (v/v) glycerol was added before flash freezing in liquid N₂ for storage at –80 °C.

Expression and purification of Nb35

DNA encoding Nb35 (described by Rasmussen et al.⁶) was cloned into a modified pET-26b expression vector with a C-terminal His-tag followed by a protein C (EDQVDPRRLIDGK) affinity tag. The resulting DNA was transformed into competent Rosetta2 (DE3) pLysS *Escherichia coli* (UC Berkeley QB3 MacroLab) and inoculated into 100 ml LB medium supplemented with 50 µg ml⁻¹ kanamycin, which was cultured overnight with 220 r.p.m. shaking at 37 °C. The following day, the starter culture was inoculated into 8 × 1 l of terrific broth supplemented with 0.1% (w/v) dextrose, 2 mM MgCl₂ and 50 µg ml⁻¹ kanamycin, which were further cultured at 37 °C with shaking. Nb35 expression was induced at OD₆₀₀ = 0.6, by addition of 40 µM isopropyl β-D-1-thiogalactopyranoside (IPTG; GoldBio) and lowering the incubator temperature to 20 °C. After 21 h of expression, cells were harvested by centrifugation and were resuspended in SET buffer comprising 200 mM tris(hydroxymethyl)aminomethane (Tris; Sigma Aldrich), pH 8, 500 mM sucrose, 0.5 mM EDTA, 20 µg ml⁻¹ leupeptin, 160 µg ml⁻¹ benzamidine and 1 U benzonase. After 30 min of stirring at room temperature, hypotonic lysis was initiated by a threefold dilution with deionized water. Following 30 min of stirring at room temperature, ionic strength was adjusted to 150 mM NaCl, 2 mM CaCl₂ and 2 mM MgCl₂ and the lysate was cleared by centrifugation at 20,000g for 30 min. The cleared lysate was incubated in batch with homemade anti-protein C antibody coupled with CNBr-Sepharose under slow rotation. The resin was extensively washed with buffer comprising 20 mM HEPES, pH 7.5, 300 mM NaCl and 2 mM CaCl₂, and Nb35 was eluted with 20 mM HEPES, pH 7.5, 100 mM NaCl, 0.2 mg ml⁻¹ protein C peptide and 5 mM EDTA. Nb35-containing fractions were concentrated in a 10-kDa MWCO spin filter (Amicon) and further purified over a Superdex S75 Increase 10/300 GL column (Cytiva) SEC column equilibrated with 20 mM HEPES, pH 7.5, and 100 mM NaCl. Fractions containing monodisperse Nb35 were concentrated and supplemented with 20% glycerol before flash freezing in liquid N₂ for storage at –80 °C.

Preparation of the active-state OR51E2–G_s complex

To prepare the OR51E2–G_s complex, a twofold molar excess of purified Gβ₁γ₂ and Nb35 was added to SEC-purified OR51E2–miniG_{s399} followed by overnight incubation on ice. The sample was concentrated on a 50-kDa MWCO spin filter (Amicon) and injected onto a Superdex 200 Increase 10/300 GL SEC column, equilibrated with 20 mM HEPES, pH

7.5, 150 mM NaCl, 0.0075% (w/v) L-MNG, 0.0025% (w/v) GDN, 0.001% (w/v) CHS and 30 mM sodium propionate. Fractions containing the monomeric OR51E2–G_s complex were concentrated on a 100-kDa MWCO spin filter immediately before cryo-EM grid preparation.

Cryo-EM vitrification, data collection and processing

Of the purified OR51E2–G_s complex, 2.75 µl was applied to glow-discharged 300 mesh R1.2/1.3 UltraAuFoil Holey gold support films (Quantifoil). Support films were plunge-frozen in liquid ethane using a Vitrobot Mark IV (Thermo Fisher) with a 10-s hold period, blot force of 0, and blotting time varying between 1 and 5 s while maintaining 100% humidity and 4 °C. Vitrified grids were clipped with Autogrid sample carrier assemblies (Thermo Fisher) immediately before imaging. Movies of OR51E2–G_s embedded in ice were recorded using a Titan Krios Gi3 (Thermo Fisher) with a BioQuantum Energy Filter (Gatan) and a K3 Direct Electron Detector (Gatan). Data were collected using SerialEM 3.8 (ref. ⁴⁶) running a 3 × 3 image shift pattern at 0° stage tilt. A nominal magnification of ×105,000 with a 100-µm objective was used in super-resolution mode with a physical pixel size of 0.81 Å per pixel. Movies were recorded using dose-fractionated illumination with a total exposure of 50 e⁻ Å⁻² over 60 frames yielding 0.833 e⁻ Å⁻² per frame.

Super-resolution movies ($n = 16,113$) were motion-corrected and Fourier-cropped to physical pixel size using UCSF MotionCor2 (ref. ⁴⁷). Dose-weighted micrographs were imported into cryoSPARC v3.2 (Structura Biotechnology⁴⁸), and contrast transfer functions (CTFs) were calculated using the patch CTF estimation tool. A threshold of CTF fit resolution of more than 5 Å was used to exclude low-quality micrographs. Particles were template picked using a 20 Å low-pass-filtered model that was generated ab initio from data collected during an earlier 200-kV screening session. Particles ($n = 8,884,130$) were extracted with a box size of 288 pixels binned to 72 pixels and sorted with the heterogeneous refinement tool, which served as 3D classification with alignment. Template volumes for each of the four classes were low-pass filtered to 20 Å and comprised an initial OR51E2–G_s volume as well as three scrambled volumes obtained by terminating the ab initio reconstruction tool before the first iteration. The resulting 1,445,818 particles were re-extracted with a box size of 288 pixels binned to 144 pixels and sorted by an additional round of heterogeneous refinement using two identical initial models and two scrambled models. Particles ($n = 776,527$) from the highest resolution reconstruction were extracted with an unbinned box size of 288 pixels and were subjected to homogeneous refinement followed by non-uniform refinement. Particles were exported using csparc2star.py from the pyem v0.5 script package⁴⁹, and an inclusion mask covering the 7TM domain of OR51E2 was generated using the Segger tool in UCSF ChimeraX v1.25 (ref. ⁵⁰) and the mask.py tool in pyem v0.5. Particles and mask were imported into Relion v3.0 (ref. ⁵¹) and sorted by several rounds of 3D classification without image alignment, in which the number of classes and tau factor were allowed to vary. The resulting 204,438 particles were brought back into cryoSPARC and subjected to non-uniform refinement. Finally, local refinement using an inclusion mask covering the 7TM domain was performed, using poses/shift Gaussian priors with standard deviation of rotational and shift magnitudes limited to 3° and 2 Å, respectively.

Model building and refinement

Model building and refinement were carried out using an AlphaFold2 (ref. ⁴⁴) predicted structure as a starting model, which was fitted into the OR51E2–G_s map using UCSF ChimeraX. A draft model was generated using ISOLDE⁵² and was further refined by iterations of real-space refinement in Phenix v1.19 (ref. ⁵³) and manual refinement in Coot v0.9.2 (ref. ⁵⁴). To identify a propionate-binding site, we considered general overlap with other class A GPCR binding pockets, general diversity of ORs within the region bounded by ECL2, TM5 and TM6, and a previous study that observed loss of activity of carboxylic acids for a R^{6×59} mutant for the OR51E2 orthologue OR51E1 (ref. ⁴²). With these constraints, we

identified a non-proteinaceous density near R262^{6×59} in sharpened maps of the OR51E2–G_s complex. The propionate model and rotamer library were generated with the PRODRG server⁵⁵ and docked using Coot to place the carboxylic acid of propionate near R262^{6×59}. The resulting model was extensively refined in Phenix. Final map-model validations were carried out using Molprobity v4.5 and EMRinger in Phenix.

Site-directed mutagenesis

Generation of OR51E2 mutants was performed as previously described⁵⁶. Forward and reverse primers coding for the mutation of interest were obtained from Integrated DNA Technologies. Two successive rounds of PCR using Phusion polymerase (F-549L, Thermo Fisher Scientific) were performed to amplify ORs with mutations. The first round of PCR generated two fragments, one containing the 5' region upstream of the mutation site and the other containing the 3' downstream region. The second PCR amplification joined these two fragments to produce a full open reading frame of the OR. PCR products with desired length were gel purified and cloned into the MluI and NotI sites of the mammalian expression vector pCI (Promega) that contains rho-tag. Plasmids were purified using the Thomas Scientific (1158P42) miniprep kit with modified protocol including phenol-chloroform extraction before column purification.

cAMP signalling assays

The GloSensor cAMP assay (Promega) was used to determine real-time cAMP levels downstream of OR activation in HEK293T cells, as previously described⁵⁷. HEK293T cells (authenticated by short tandem repeat profiling and tested negative for mycoplasma contamination) were cultured in minimum essential medium (MEM; Corning) supplemented by 10% FBS (Gibco), 0.5% penicillin–streptomycin (Gibco) and 0.5% amphotericin B (Gibco). Cultured HEK293T cells were plated the day before transfection at 1/10 of 100% confluence from a 100-mm plate into 96-well plates coated with poly-D-lysine (Corning). For each 96-well plate, 10 µg pGloSensor-2OF plasmid (Promega) and 75 µg of rho-tagged OR in the pCI mammalian expression vector (Promega) were transfected 18–24 h before odorant stimulation using Lipofectamine 2000 (11668019, Invitrogen) in MEM supplemented by 10% FBS. On stimulation day, plates were injected with 25 µl of GloSensor substrate (Promega) and incubated for 2 h in the dark at room temperature and in an odour-free environment. Odorants were diluted to the desired concentration in CD293 medium (Gibco) supplemented with copper (30 µM CuCl₂; Sigma-Aldrich) and 2 mM L-glutamine (Gibco) and pH adjusted to 7.0 with a 150 mM solution of sodium hydroxide (Sigma-Aldrich). After injecting 25 µl of odorants in CD293 medium into each well, GloSensor luminescence was immediately recorded for 20 cycles of monitoring over a total period of 30 min using a BMG Labtech POLARStar Optima plate reader. The resulting luminescence activity was normalized to a vector control lacking any OR, and the OR response was obtained by summing the response from all 20 cycles to determine an area under the curve. Dose-dependent responses of ORs were analysed by fitting a least squares function to the data using GraphPrism 9.

Evaluating cell-surface expression

Flow cytometry was used to evaluate cell-surface expression of ORs as previously described⁵⁸. HEK293T cells were seeded onto 35-mm plates (Greiner Bio-One) with approximately 3.5×10^5 cells (25% confluence). The cells were cultured overnight. After 18–24 h, 1,200 ng of ORs tagged with the first 20 amino acids of human rhodopsin (rho-tag) at the N-terminal ends⁵⁹ in pCI (Promega) and 30 ng eGFP were transfected using Lipofectamine 2000 (11668019, Invitrogen). 18–24 h after transfection, the cells were detached and resuspended using Cell stripper (Corning) and then transferred into 5-ml round bottom polystyrene tubes (Falcon) on ice. The cells were spun down at 4 °C and resuspended in PBS (Gibco) containing 15 mM NaN₃ (Sigma-Aldrich) and 2% FBS

Article

(Gibco). They were stained with 1/400 (v/v) of primary antibody mouse anti-rhodopsin clone 4D2 (MABN15, Sigma-Aldrich) and allowed to incubate for 30 min, then washed with PBS containing 15 mM Na₃, and 2% FBS. The cells were spun again and then stained with 1/200 (v/v) of the phycoerythrin-conjugated donkey anti-mouse F(ab')2 fragment antibody (715-116-150, Jackson Immunologicals) and allowed to incubate for 30 min in the dark. To label dead cells, 1/500 (v/v) of 7-amino-actinomycin D (129935, Calbiochem) was added. The cells were then immediately analysed using a BD FACSCanto II flow cytometer with gating allowing for GFP-positive, single, spherical, viable cells, and the measured phycoerythrin fluorescence intensities were analysed and visualized using Flowjo v10.8.1. Normalizing the cell-surface expression levels of the OR51E2 mutants was performed using wild-type OR51E2, which showed robust cell-surface expression, and empty plasmid pCI, which demonstrated no detectable cell-surface expression.

MD simulations

All MD simulations were performed using the GROMACS package⁶⁰ (version 2021) with the CHARMM36m forcefield⁶¹ starting from the OR51E2 EM structure with and without propionate. The G protein was removed in all of these simulations. The GPCR structures were prepared by Maestro (v13.0.135, Schrödinger) ‘protein preparation wizard’ module⁶². The missing side chains and hydrogen atoms were added. Furthermore, protein chain termini were capped with neutral acetyl and methylamide groups, and histidine protonated states were assigned, after which minimization was performed. The simulation box was created using CHARMM-GUI⁶³. We used the PPM 2.0 function of OPM (orientation of proteins in membranes)⁶⁴ structure of OR51E2 for alignment of the transmembrane helices of protein structure and inserted into a 75% palmitoyl-oleoyl-phosphatidylcholine (POPC)-25% cholesteryl hemisuccinate deprotonated (CHSD) bilayer. The CHSDs were placed around the GPCR structure. The TIP3P water model was used for solvation, and 0.15 M potassium chloride ions were added for neutralization. The final system dimensions were about 85 Å × 85 Å × 115 Å. The system was minimized with position restraints (10 kcal per mol per Å²) on all heavy atoms of GPCR and ligand, followed by a 1-ns heating step, which raised the temperature from 0 K to 310 K in NVT ensemble with a Nosé–Hoover thermostat⁶⁵. Then, we performed a single long equilibration for lipid and solvent (1,000 ns) in NPT ensemble. During the heating step and the long equilibration, position restraints were placed of 10 kcal per mol per Å² applied on the receptor, propionate and POPC–CHSD for the first 1 ns. Later, the restraint on lipids was reduced from 5 kcal per mol per Å² to 0 kcal per mol per Å² in steps of 1 kcal with 5 ns of simulations per step. Then, POPC–CHSD were allowed to freely move during the rest of the long equilibration and the final snapshot was used as the initial conformation for equilibrating the protein and ligand. The position restraints were applied on the protein (backbone and side chain) and ligand starting at 5 kcal per mol per Å² reducing to 0 kcal per mol per Å² in steps of 1 kcal per mol per Å² with 5 ns of simulation per step. The last snapshot of the equilibration step was used as initial conformation for five production runs with random seeds. This snapshot was also used as reference conformation for all of the root-mean-square deviation (RMSD) in coordinates. The pressure was controlled using the Parrinello–Rahman method⁶⁶, and the simulation system was coupled to a 1-bar pressure bath. In all simulations, the LINCS algorithm was applied on all bonds and angles of waters, with a 2-fs time step used for integration. We used a cut-off of 12 Å for non-bond interaction and the particle mesh Ewald method⁶⁷ to treat long-range L-J interaction. The MD snapshots were stored at every 20-ps interval. Trajectories were visualized with VMD v1.9.3 and PyMOL (Molecular Graphics System v2.5, Schrödinger) and analysed using the GROMACS package (v2016/2019). All MD analysis was done on the aggregated trajectories for each system from five runs (total 5 × 1 μs = 5 μs). Heatmaps and other MD-related plots were generated with Graphpad Prism 9, whereas structural figures were generated using

PyMOL. Summary of the statistics for all the properties (residue distances, rotamer angle and RMSD in coordinates) calculated from the aggregated MD simulation trajectories are presented in Supplementary Tables 1–6.

MD analysis

Ligand–receptor interactions. Contact frequencies were calculated using the ‘get_contacts’ module (<https://getcontacts.github.io/>). The following interaction types were calculated between ligand and receptor: hydrogen bonds, hydrophobic and van der Waals interactions.

Calculation of residue distances. For the distance between two residues, we used gmx mindist (GROMACS package 2016/2019), which calculates the minimal distance between two atoms (for example, side chain, Cα, oxygens and nitrogens) of one of each residue over time. Distance analysis on the static structures was done using the measurement tool in PyMOL. Chosen atoms for distance calculations are described in each legend.

Rotamer analysis of F250. For the rotamer analysis of residues of interest, we used the VMD tcl script ‘Calculate_dihedrals’ (https://github.com/ajasja/calculate_dihedrals).

Representative snapshots and conformational clustering. We show the final snapshot from every replicate simulation for each system (end of 1,000 ns of simulation for each replicate) in Figs. 2f, 4i and 5b, and in Extended Data Fig. 9a–c as a single frame after 1,000 ns of simulation time. We also performed an unbiased analysis of the structural changes using unsupervised clustering of simulation ensembles to examine the conformational heterogeneity of MD simulations. We clustered the aggregated trajectories by applying the single-linkage method on the transmembrane helix backbone atoms (using the gmx cluster function in the GROMACS package 2016/2019). An RMSD cut-off for clustering was set at 0.8 Å for propionate-bound wild-type OR51E2 simulations, 0.85 Å for no-ligand wild-type OR51E2 simulations and 0.85 Å for no-ligand Q181^{45×53}D OR51E2 simulations. Resulting cluster populations are shown in Supplementary Table 7. The top populated cluster (or clusters) from the clustering analysis (that covered more than 90% of the MD snapshots) were used to extract the representative snapshots for each conformational cluster shown in Supplementary Fig. 1. The structural changes observed in the last snapshot of each replicate were similar to the changes observed in the cluster representative structures, as illustrated in Supplementary Fig. 1. Thus, an unbiased approach of analysing the large-scale MD simulation ensemble led to similar conclusions on the conformational changes deduced from the last snapshot.

RMSD. The gmx rms (GROMACS package 2016/2019) function was used to determine whether simulations were stable. We used the transmembrane backbone of OR51E2 by selecting the following residues: 23–50 (TM1), 57–86 (TM2), 93–126 (TM3), 137–164 (TM4), 191–226 (TM5), 230–264 (TM6) and 269–294 (TM7). As reference, we used the equilibrated MD structure of propionate bound, apo and Q181^{45×53}D OR51E2. To assess the stability of the ligand in the binding pocket over time, the RMSD of propionate was calculated using the equilibrated MD structure of bound propionate as a reference.

Generating OR51E2-mutant structural models, docking of C6 and C8 ligands and procedure for calculating the volume of the ligand-binding pocket. The volume and surface area of the propionate-binding pocket in OR51E2 was calculated using the Maestro SiteMap module^{68,69}. Three structures were used for the volume calculation: (1) the OR51E2 cryo-EM structure bound to propionate, (2) the OR51E2(L158A) model bound to hexanoate, and (3) the OR51E2(F155A) model bound to octanoate. To prepare the L158A and F155A structural

models, we used the Maestro mutation function to introduce the substitutions onto the cryo-EM structure of OR51E2; these models were then energy minimized using the ProteinPreparationWizard module using default parameters⁶². We then used Maestro Glide Docking^{70–72} to dock hexanoate and octanoate into the resulting models of OR51E2(L158A) and OR51E2(F155A), respectively. We prepared the docking grid box for both OR51E2(L158A) and OR51E2(F155A) by defining a box centred at propionate, with a box length of 2.5 nm. Glide ligand docking was performed using XP precision and default parameters to yield a model for OR51E2(L158A) bound to hexanoate and OR51E2(F155A) bound to octanoate. To calculate ligand-binding site volumes using the SiteMap module, we defined the ligand-binding pocket as the residues within 6 Å around selected ligand (propionate, hexanoate or octanoate) with at least 15 site points (probes) per reported site. The grid size for the probes was set to 0.35 Å. Using this approach, the calculated volumes for wild-type OR51E2, OR51E2(L158A) and OR51E2(F155A) were 31 Å³, 68 Å³ and 90 Å³, respectively.

Phylogenetic tree

A phylogenetic tree of human class A GPCRs was made by analysing 677 full-length sequences. Of these, 390 sequences were from ORs (56 class I ORs and 334 class II ORs), whereas 287 sequences were from non-olfactory class A GPCRs. Sequences were aligned with ClustalX/ClustalW 2.1 (ref.⁷³) on Jalview 2.11.2.5 (ref.⁷⁴). In the transmembrane regions, motifs conserved in all class A GPCRs (TM1: GN^{1×50}; TM2: LxxxD^{2×50} and P^{2×59}; TM3: C^{3×25} and DR^{3×50}Y; TM4: W^{4×50}; TM5: P^{5×50} and Y^{5×58}xxI^{5×61}; TM7: NP^{7×50}xxY) were aligned. The case of TM6 is less obvious as ORs and non-olfactory GPCRs do not share a common amino acid motif in this helix. As proposed originally by de March et al.³³, and supported by structural comparison of OR51E2 to β₂AR, we aligned the CWLP^{6×50} motif of the non-olfactory class A GPCRs with the FYGx^{6×50} OR motif.

This structure-based alignment is consistent with generic residue numbering provided in the latest iteration of GPCRdb⁷⁵. For helix 8, we initially aligned the conserved residue F^{8×50} from non-olfactory class A GPCRs and the corresponding residue hydrophobic residues V/I/M at position 8×50 in ORs (I^{8×50} in OR51E2). Further confidence in helix 8 alignment was gained by alignment of positions 8×46 (R in 84% of ORs), 8×47 (N in 84% of ORs), 8×48 (K in 69% of ORs) and 8×53 (A in 76% of ORs). Alignment of the intracellular and extracellular loops was also driven by conserved residues when available. For the intracellular loops (ICLs), L^{12×50} in ICL1 and P^{34×50} in ICL2 are conserved between ORs and non-olfactory class A GPCRs. ICL3 has substantial variation in non-olfactory class A GPCRs. In ORs, ICL3 is very short, so S^{6×26} (76% conserved in ORs) was used to align the intracellular end of TM6. For the ECLs, ECL1 does not contain residues common between ORs and non-olfactory class A GPCRs. ECL1 was therefore aligned by matching the conserved residue W^{23×50} in non-olfactory class A GPCR with the residues K, R and N, which are moderately conserved in ORs (52%, 15% and 9%, respectively). This alignment was further supported with the more conserved position 23×52 (I in 94% of ORs) and 23×53 (S in 79% of ORs). For ECL2, we used C45×50, which is conserved between non-olfactory class A GPCRs and ORs; in addition, the OR-specific residues C^{45×40} and C^{45×60} were used to align OR sequences. Finally, ECL3 is not conserved within the class A GPCR family so was only aligned to fit between TM6 and TM7. On R studio 202.07.01, alignment reading and matrix of distance between sequences (by sequence identity) calculation were performed with the Biostrings 2.66.0 (ref.⁷⁶) and seqinr 4.2-23 (ref.⁷⁷) packages. Neighbour-joining tree and tree visualization were realized with packages ape 5.6-2 (ref.⁷⁸) and ggtree 3.6.2 (ref.⁷⁹), and the tree was plotted unrooted with the daylight method.

Reporting summary

Further information on research design is available in the Nature Portfolio Reporting Summary linked to this article.

Data availability

Coordinates for the propionate OR51E2–G_s complex have been deposited in the RCSB Protein Data Bank under accession code 8F76. EM density maps for OR51E2–G_s and the 7TM domain of OR51E2 have been deposited in the Electron Microscopy Data Bank under accession codes EMD-28896 and EMD-28900, respectively. The MD simulation trajectories for apo OR51E2, OR51E2 bound to propionate, and OR51E2–Q181^{45×53}D mutant have been deposited in the GPCRdb database under accession codes 1244, 1245, and 1246, respectively. This paper makes use of RCSB Protein Data Bank accession codes 3SN6, 4LDO and 6FUF.

45. Staus, D. P. et al. Sortase ligation enables homogeneous GPCR phosphorylation to reveal diversity in β-arrestin coupling. *Proc. Natl Acad. Sci. USA* **115**, 3834–3839 (2018).
46. Mastronarde, D. N. SerialEM: a program for automated tilt series acquisition on Tecnai microscopes using prediction of specimen position. *Microsc. Microanal.* **9**, 1182–1183 (2003).
47. Zheng, S. Q. et al. MotionCor2: anisotropic correction of beam-induced motion for improved cryo-electron microscopy. *Nat. Methods* **14**, 331–332 (2017).
48. Punjani, A., Rubinstein, J. L., Fleet, D. J. & Brubaker, M. A. cryoSPARC: algorithms for rapid unsupervised cryo-EM structure determination. *Nat. Methods* **14**, 290–296 (2017).
49. Asarnow, D., Palovcak, E. & Cheng, Y. Asarnow/pyem: UCSF Pyem v0.5. Zenodo https://doi.org/10.5281/zenodo.3576630 (2019).
50. Pettersen, E. F. et al. UCSF ChimeraX: structure visualization for researchers, educators, and developers. *Protein Sci.* **30**, 70–82 (2021).
51. Scheres, S. H. W. RELION: implementation of a Bayesian approach to cryo-EM structure determination. *J. Struct. Biol.* **180**, 519–530 (2012).
52. Croll, T. I. ISOLDE: a physically realistic environment for model building into low-resolution electron-density maps. *Acta Crystallogr. D Struct. Biol.* **74**, 519–530 (2018).
53. Adams, P. D. et al. PHENIX: a comprehensive Python-based system for macromolecular structure solution. *Acta Crystallogr. D Biol. Crystallogr.* **66**, 213–221 (2010).
54. Emsley, P. & Cowtan, K. Coot: model-building tools for molecular graphics. *Acta Crystallogr. D Biol. Crystallogr.* **60**, 2126–2132 (2004).
55. Schüttelkopf, A. W. & van Aalten, D. M. F. PRODRG: a tool for high-throughput crystallography of protein–ligand complexes. *Acta Crystallogr. D Biol. Crystallogr.* **60**, 1355–1363 (2004).
56. Bushdid, C., de March, C. A., Matsunami, H. &olebiowski, J. Numerical models and in vitro assays to study odorant receptors. *Methods Mol. Biol.* **1820**, 77–93 (2018).
57. Zhang, Y., Pan, Y., Matsunami, H. & Zhuang, H. Live-cell measurement of odorant receptor activation using a real-time cAMP assay. *J. Vis. Exp.* **128**, 55831 (2017).
58. Zhuang, H. & Matsunami, H. Evaluating cell-surface expression and measuring activation of mammalian odorant receptors in heterologous cells. *Nat. Protoc.* **3**, 1402–1413 (2008).
59. Krautwurst, D., Yau, K. W. & Reed, R. R. Identification of ligands for olfactory receptors by functional expression of a receptor library. *Cell* **95**, 917–926 (1998).
60. Berendsen, H. J. C., van der Spoel, D. & van Drunen, R. GROMACS: a message-passing parallel molecular dynamics implementation. *Comput. Phys. Commun.* **91**, 43–56 (1995).
61. Huang, J. et al. CHARMM36m: an improved force field for folded and intrinsically disordered proteins. *Nat. Methods* **14**, 71–73 (2017).
62. Madhavi Sastry, G., Adzhigirey, M., Day, T., Annabhipmoju, R. & Sherman, W. Protein and ligand preparation: parameters, protocols, and influence on virtual screening enrichments. *J. Comput. Aided Mol. Des.* **27**, 221–234 (2013).
63. Jo, S., Kim, T., Iyer, V. G. & Im, W. CHARMM-GUI: a web-based graphical user interface for CHARMM. *J. Comput. Chem.* **29**, 1859–1865 (2008).
64. Lomize, M. A., Pogozheva, I. D., Joo, H., Mosberg, H. I. & Lomize, A. L. OPM database and PPM web server: resources for positioning of proteins in membranes. *Nucleic Acids Res.* **40**, D370–D376 (2012).
65. Evans, D. J. & Holian, B. L. The Nose–Hoover thermostat. *J. Chem. Phys.* **83**, 4069–4074 (1985).
66. Parrinello, M. & Rahman, A. Polymorphic transitions in single crystals: a new molecular dynamics method. *J. Appl. Phys.* **52**, 7182–7190 (1981).
67. Darden, T., York, D. & Pedersen, L. Particle mesh Ewald: an N-log(N) method for Ewald sums in large systems. *J. Chem. Phys.* **98**, 10089–10092 (1993).
68. Halgren, T. New method for fast and accurate binding-site identification and analysis. *Chem. Biol. Drug Des.* **69**, 146–148 (2007).
69. Halgren, T. A. Identifying and characterizing binding sites and assessing druggability. *J. Chem. Inf. Model.* **49**, 377–389 (2009).
70. Friesner, R. A. et al. Extra precision glide: docking and scoring incorporating a model of hydrophobic enclosure for protein–ligand complexes. *J. Med. Chem.* **49**, 6177–6196 (2006).
71. Halgren, T. A. et al. Glide: a new approach for rapid, accurate docking and scoring. 2. Enrichment factors in database screening. *J. Med. Chem.* **47**, 1750–1759 (2004).
72. Friesner, R. A. et al. Glide: a new approach for rapid, accurate docking and scoring. 1. Method and assessment of docking accuracy. *J. Med. Chem.* **47**, 1739–1749 (2004).
73. Larkin, M. A. et al. Clustal W and Clustal X version 2.0. *Bioinformatics* **23**, 2947–2948 (2007).
74. Waterhouse, A. M., Procter, J. B., Martin, D. M. A., Clamp, M. & Barton, G. J. Jalview version 2—a multiple sequence alignment editor and analysis workbench. *Bioinformatics* **25**, 1189–1191 (2009).
75. Pándy-Szekeres, G. et al. GPCRdb in 2023: state-specific structure models using AlphaFold2 and new ligand resources. *Nucleic Acids Res.* **51**, D395–D402 (2022).
76. Pagès, H., Aboyou, P., Gentleman, R. & DebRoy, S. Biostrings: efficient manipulation of biological strings. R package version 2.66.0 (Bioconductor, 2022).

Article

77. Charif, D. & Lobry, J. R. in *Structural Approaches to Sequence Evolution: Molecules, Networks, Populations* (eds Bastolla, U. et al.) 207–232 (Springer, 2007).
78. Paradis, E. & Schliep, K. ape 5.0: An environment for modern phylogenetics and evolutionary analyses in R. *Bioinformatics* **35**, 526–528 (2019).
79. Xu, S. et al. Ggtree: a serialized data object for visualization of a phylogenetic tree and annotation data. *iMeta* **1**, e56 (2022).
80. Dang, S. et al. Cryo-EM structures of the TMEM16A calcium-activated chloride channel. *Nature* **552**, 426–429 (2017).

Acknowledgements We thank D. Toso at Cal-Cryo at QB3-Berkeley for help in microscope operation and data collection; and H.M., C.A.d.M. and J.T. thank M. J. Ni and H.-Y. Lu for their technical support. This work was supported by the US NIH grant R01DC020353 (to H.M., N.V. and A.M.) and K99DC018333 (to C.A.d.M.). Cryo-EM equipment at UCSF is partially supported by NIH grants S10OD020054 and S10OD021741. This project was funded by the UCSF Program for Breakthrough Biomedical Research, funded in part by the Sandler Foundation. A.M. acknowledges support from the Edward Mallinckrodt Jr Foundation and the Vallee Foundation, and is a Chan Zuckerberg Biohub Investigator. H.M. acknowledges support from NSF/CIHR/DFG/FRQ/UKRI-MRC Next Generation Networks for Neuroscience Program (award #2014217).

Author contributions C.B.B., C.A.d.M., W.J.C.v.d.V., N.V., H.M. and A.M. designed the study. C.B.B. cloned constructs, prepared baculoviruses, expressed and purified G protein-complexing reagents, and optimized large-scale production of OR51E2. C.B.B. worked out conditions to biochemically purify and stabilize the propionate-bound OR51E2-G_s complex, and identified optimal cryo-EM grid preparation procedures following screening, collection and processing of 200-kV cryo-EM data. B.F. and A.M. performed 300-kV cryo-EM data collection. C.B.B. determined high-resolution cryo-EM maps by extensive image processing with input from A.M.

A.M. and C.B.B. built, refined models of propionate-bound OR51E2 in complex with G_s and Nb35. C.B.B. and A.M. analysed cryo-EM data and models, and prepared figures and tables. C.A.d.M. and J.T. analysed OR models and sequences to design and clone OR mutants, performed GloSensor signalling experiments for OR functional activity and generated OR cell-surface expression data by flow cytometry with input from H.M. C.A.d.M. and J.T. analysed and prepared figures and tables for signalling and flow cytometry data. C.A.d.M. built the phylogenetic tree of ORs and non-olfactory class A GPCRs. N.M. set up and performed MD simulations and ligand docking, and performed binding pocket volume calculations. W.J.C.v.d.V. analysed simulation trajectories and prepared figures describing simulation data. W.J.C.v.d.V., N.M. and N.V. provided mechanistic insight from simulation data. C.L.d.T. performed bioinformatic analysis of OR and non-olfactory class A GPCR conservation. L.L. and C.B.B. performed pilot GloSensor signalling studies in suspension cells. C.B.B., C.A.d.M. and A.M. wrote an initial draft of the manuscript and generated figures with contributions from all authors. Further edits to the manuscript were provided by W.J.C.v.d.V., N.M., N.V. and H.M. The overall project was supervised by N.V., H.M. and A.M.

Competing interests H.M. has received royalties from Chemcom, research grants from Givaudan and consultant fees from Kao.

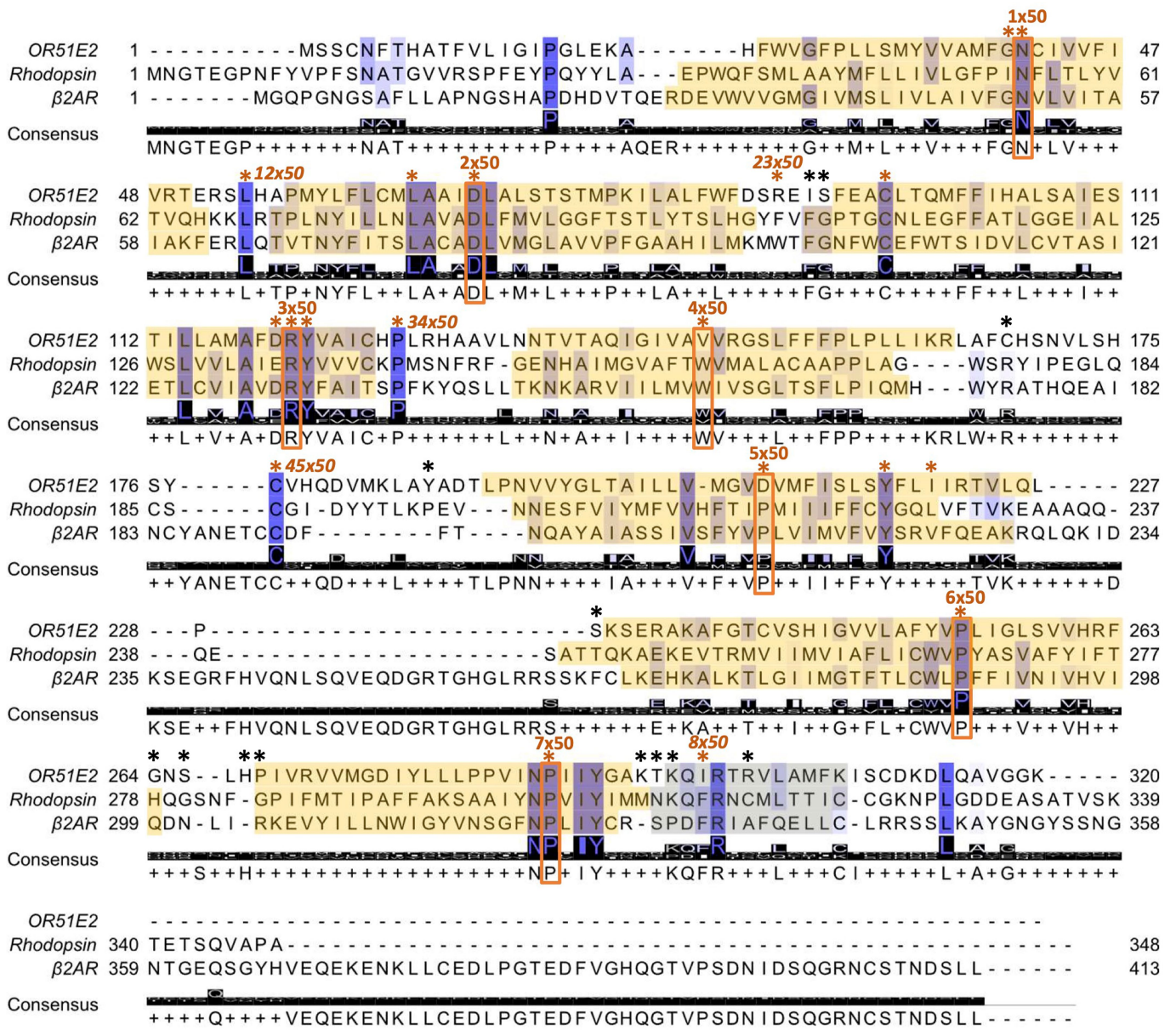
Additional information

Supplementary information The online version contains supplementary material available at <https://doi.org/10.1038/s41586-023-05798-y>.

Correspondence and requests for materials should be addressed to Nagarajan Vaidehi, Hiroaki Matsunami or Aashish Manglik.

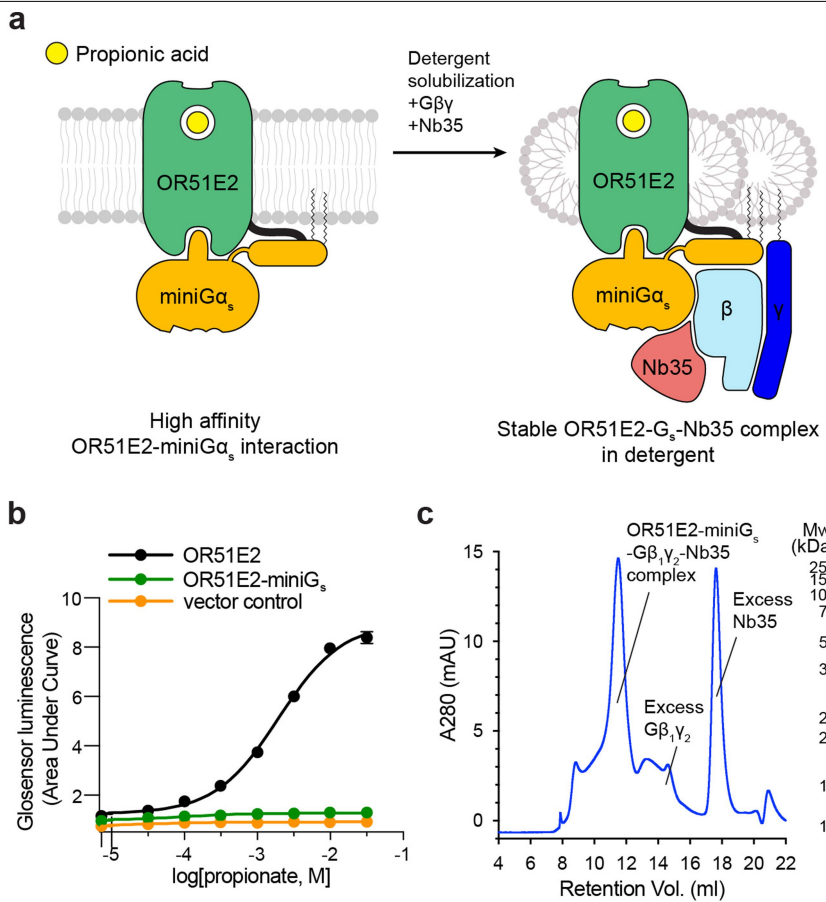
Peer review information *Nature* thanks David Gloriam and the other, anonymous, reviewer(s) for their contribution to the peer review of this work. Peer reviewer reports are available.

Reprints and permissions information is available at <http://www.nature.com/reprints>.



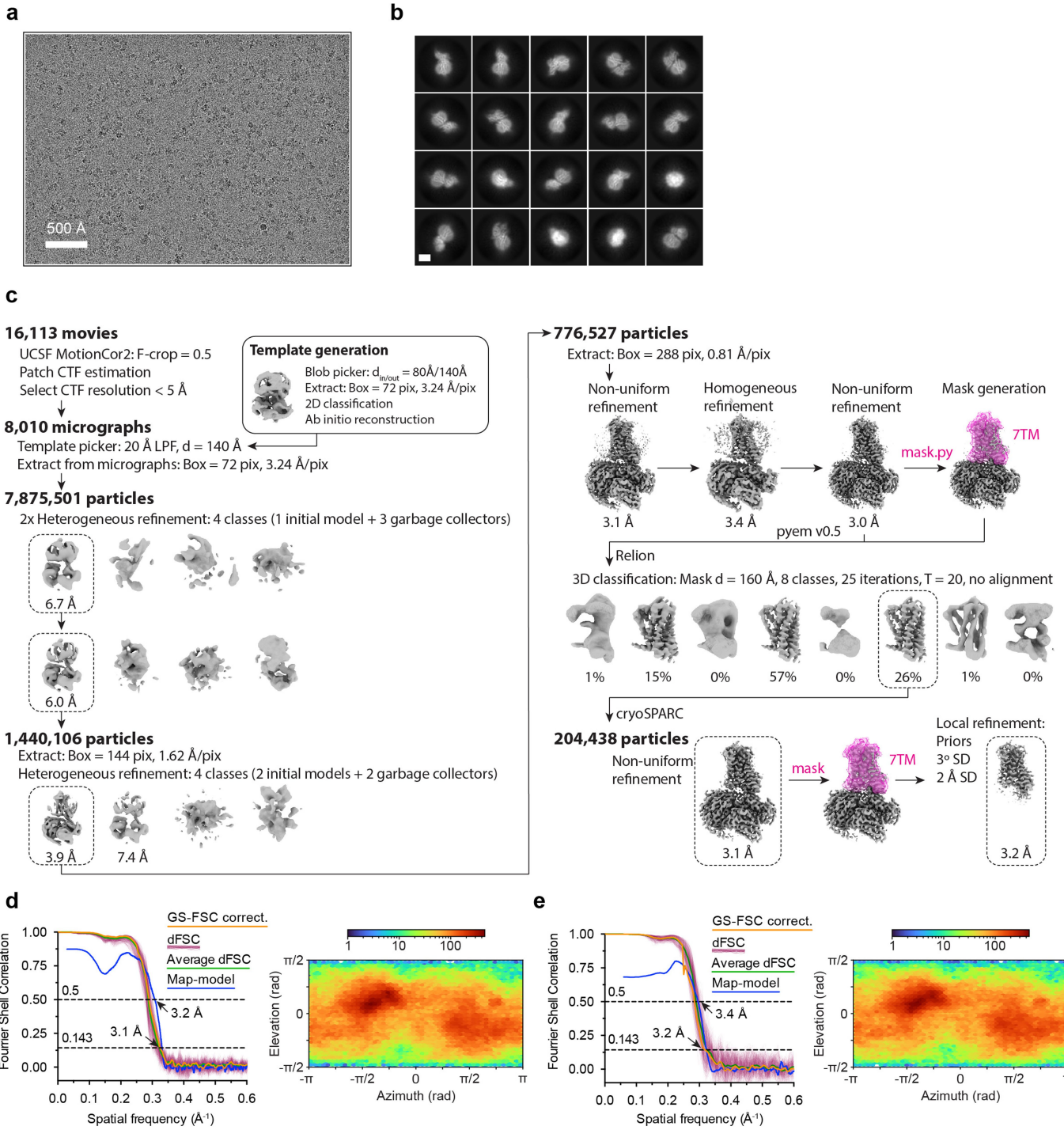
Extended Data Fig. 1 | Alignment of ORS1E2, rhodopsin and β 2 adrenergic receptor (β 2AR) amino acid sequences as described in part by de March et al.³³ and implemented on GPCRdb⁷. Conservation is highlighted from low (white) to high (dark blue) and the consensus amino acid is shown. Transmembrane domains are boxed in yellow. The most conserved residue in class A GPCRs for each transmembrane domain is boxed and labeled in orange.

Residues used to align OR and Class A GPCR sequences are highlighted by asterisks, which are colored orange when the residue is common to all Class A GPCRs and black when it is specific to ORs. The most conserved residues used for numbering of the intracellular and extracellular loops are also indicated in italic when available. Generic numbers follow the revised Ballesteros-Weinstein numbering for Class A GPCRs^{32,34}.



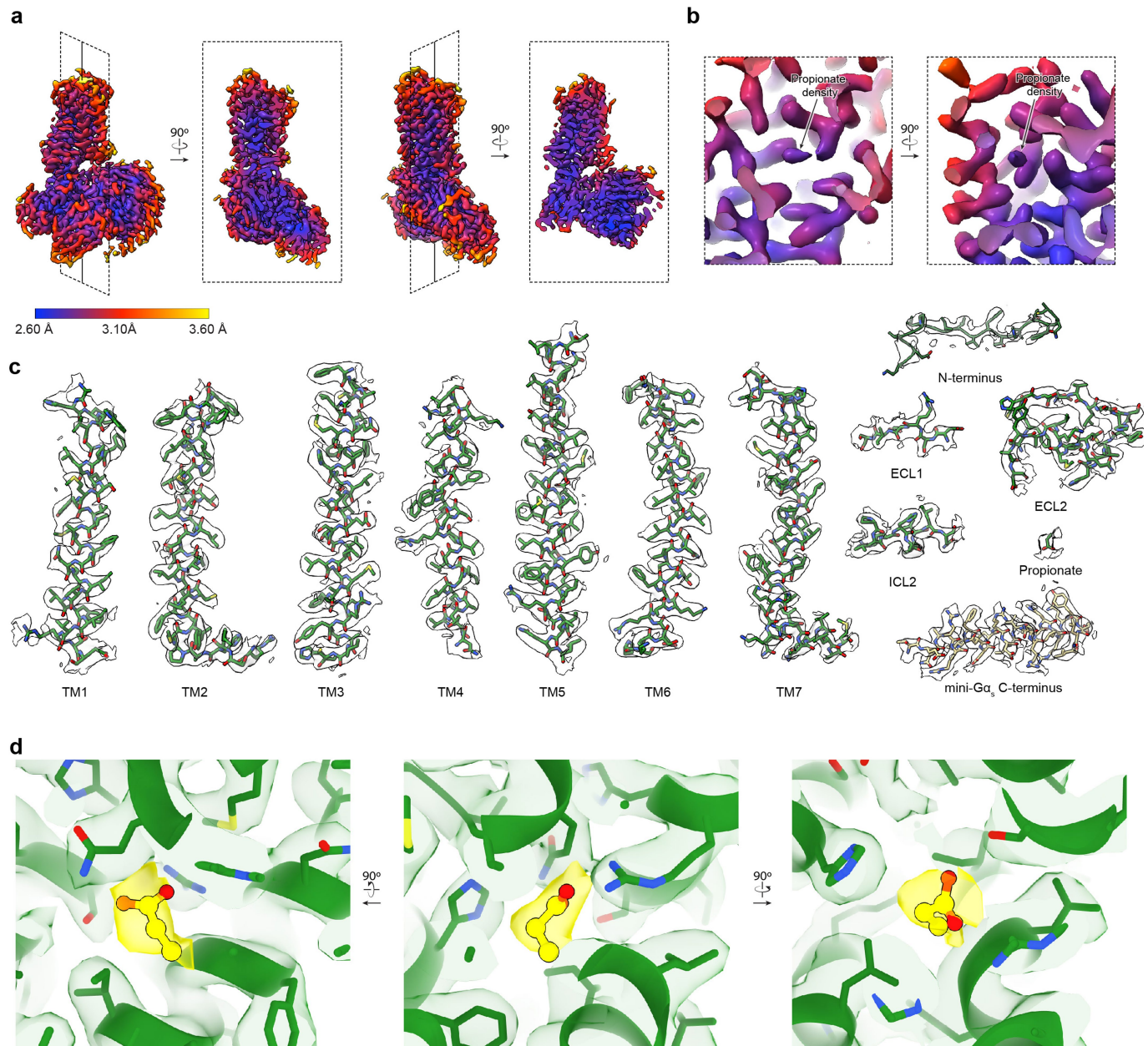
Extended Data Fig. 2 | Biochemical preparation of OR51E2-G^s complex bound to propionate. **a)** Schematic outlining the strategy for stabilization and purification of the activated OR51E2-G^s complex bound to propionate. **b)** GloSensor cAMP assay demonstrating that fusion of miniG^s to OR51E2 blocks activation of endogenous G^s in response to treatment with propionate, suggesting that miniG^s couples to the OR51E2 transmembrane core. Data points are the mean of analytical replicates from a representative experiment.

Error bars represent the standard deviation between replicates ($n = 4$). **c)** Size-exclusion chromatogram of purified OR51E2-G^s-Nb35 complex used for structure determinations shown together with a representative SDS-PAGE gel analysis of the collected fraction containing the OR51E2-G^s-Nb35 complex. We observe two bands for OR51E2, likely due to heterogeneous glycosylation of the receptor N-terminus.



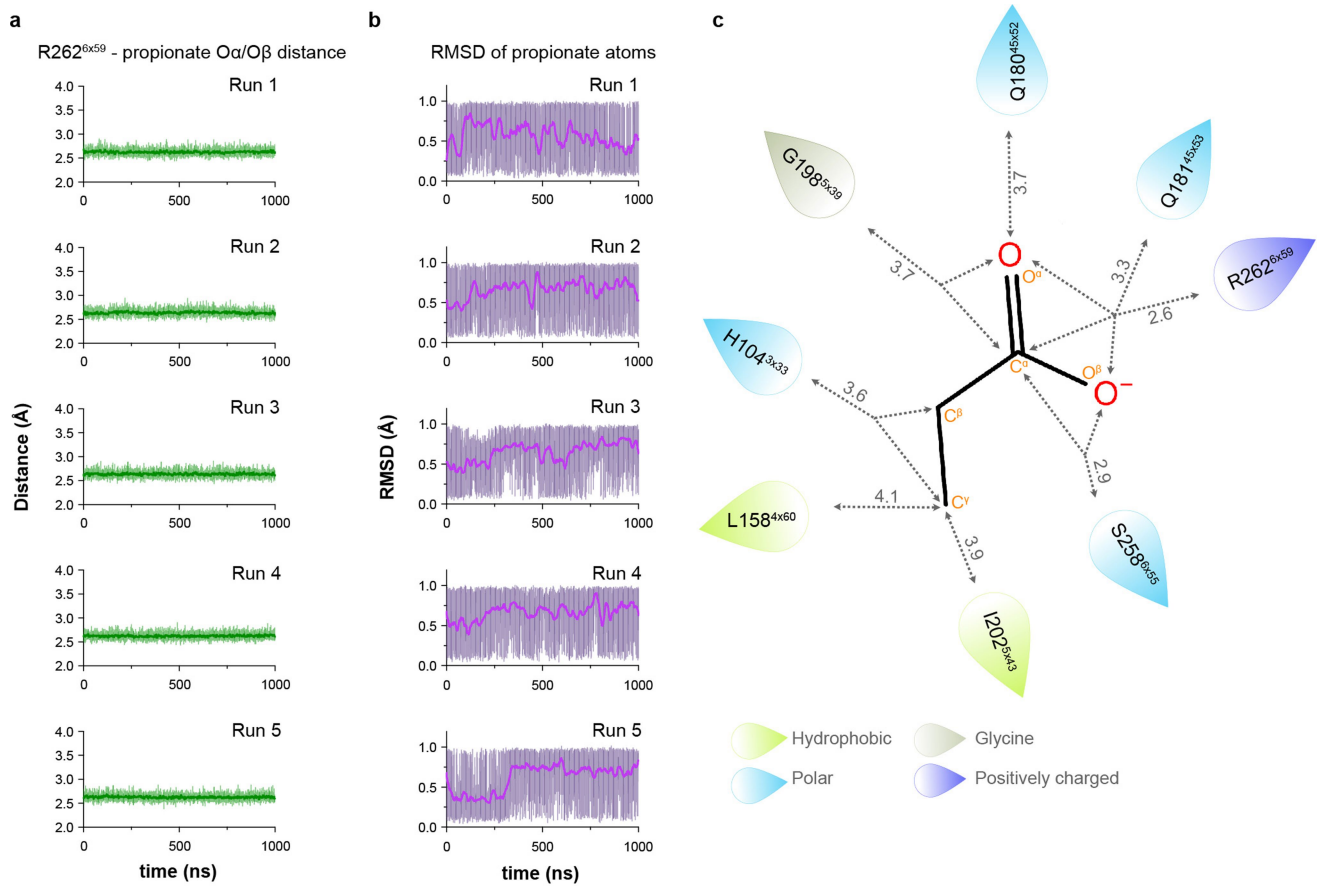
Extended Data Fig. 3 | Cryo-EM data processing for OR51E2-G_s.
a) A representative cryo-EM micrograph from the curated OR51E2-G_s dataset ($n = 8,010$) obtained from a Titan Krios microscope. **b**) A subset of highly populated, reference-free 2D-class averages are shown. Scale bar is 50 Å.
c) Schematic showing the image processing workflow for OR51E1-G_s. Initial processing was performed using UCSF MotionCor2 and cryoSPARC. Particles were then transferred using the pyem script package⁴⁹ to RELION for alignment-free 3D classification. Finally, particles were processed in cryoSPARC using the non-uniform and local refinement tools. Dashed boxes

indicate selected classes, and 3D volumes of classes and refinements are shown along with global Gold-standard Fourier Shell Correlation (GSFSC) resolutions. **d,e**) Map validation for the OR51E2-G_s (**d**) globally refined, and (**e**) locally refined cryo-EM maps. GSFSC curves are calculated in cryoSPARC, and shown together with directional FSC (dFSC) curves generated with dfsc.0.0.1.py as previously described⁸⁰. Map-model correlations calculated in the Phenix suite are also shown. Arrows indicate map and map-model resolution estimates at 0.143 and 0.5 correlation respectively. Euler angle distributions calculated in cryoSPARC are also provided for each map.



Extended Data Fig. 4 | Cryo-EM density and atomic model. **a**) Orthogonal views of local resolution for the globally refined map of OR51E2-G_s calculated with the local resolution estimation tool in cryoSPARC. **b**) Close-up view showing the local resolution of the propionate binding site. **c**) Representative cryo-EM densities from the 3D reconstruction of OR51E2 from a sharpened,

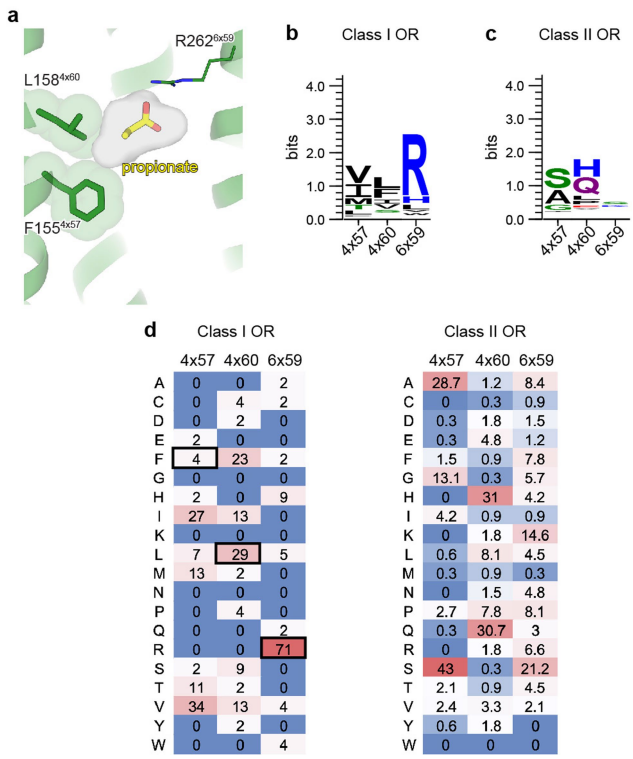
globally refined map of OR51E2-G_s at a map threshold of 0.635. Shown are the transmembrane helices and loop regions of OR51E2 as well as the C-terminal helix of miniGα_s. **d**) Close-up view of cryo-EM density (yellow sticks and density) supporting propionate binding pose using a sharpened map locally refined around only the 7TM domain of OR51E2 at map threshold of 1.0.



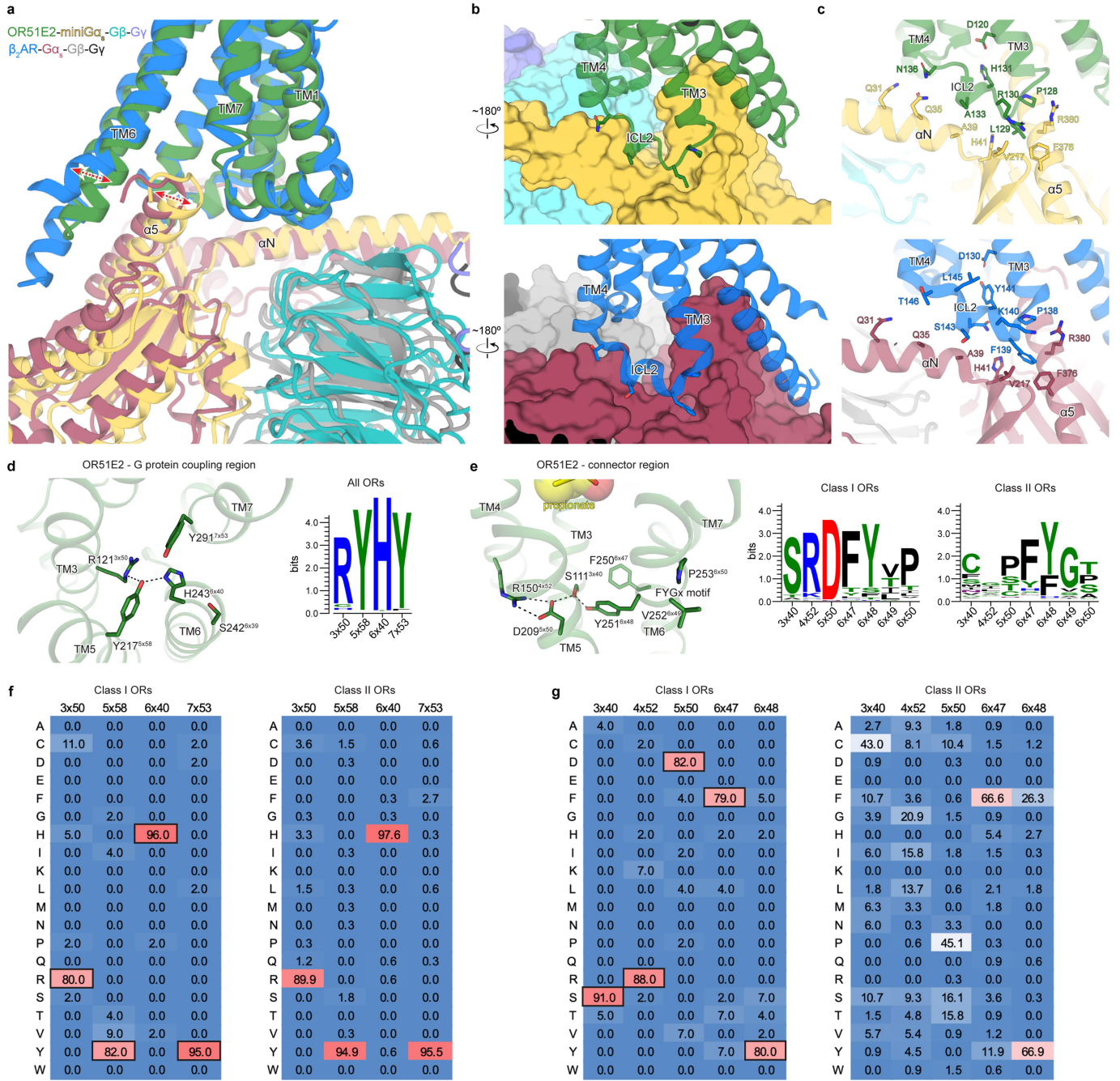
Extended Data Fig. 5 | Interactions between propionate and OR51E2 in molecular dynamics simulations. **a)** Minimum distance plot between R262^{6×59} and propionate from 5 independent runs at different velocities (top to bottom). Minimum distance was measured between guanidinium nitrogens of R262^{6×59} and oxygens of propionate. Thick trace represents smoothed values with an averaging window of 8 nanoseconds; thin trace represents unsmoothed values. **b)** Root-mean-square deviation (RMSD) values of production simulation runs for propionate calculated with reference to the equilibrated structure of OR51E2 prior to 1 μ s production simulation from 5 independent runs at

different velocities (top to bottom). **c)** Minimum distances (\AA) between ligand heavy atoms and residue side chain heavy atoms (hydrogen bond and van der Waals contacts combined) are shown in gray. Gray dashed arrows highlight the interactions made between a certain receptor residue and ligand atom(s). All distances are shown as means from $n = 5$ independent runs (at different velocities) each 1 μ s long. Standard deviation of measurement for each of the residue-ligand distance are as follows: 0.03 \AA (R262^{6×59}), 0.10 \AA (S258^{8×55}), 0.16 \AA (I202^{5×43}), 0.12 \AA (G198^{5×39}), 0.23 \AA (Q181^{45×53}), 0.23 \AA (H180^{45×52}), 0.25 \AA (L158^{4×60}), and 0.14 \AA (H104^{3×33}).

Article



Extended Data Fig. 6 | Conservation of residues within the odorant binding pocket. **a)** View of propionate-contacting residues. Conservation weblogo of key residues in Class I **(b)** and Class II ORs **(c)**. **d)** The percentage of receptors harboring a given amino acid at each position are shown for all human Class I and Class II ORs. OR51E2 residues at each position are indicated by a black box.

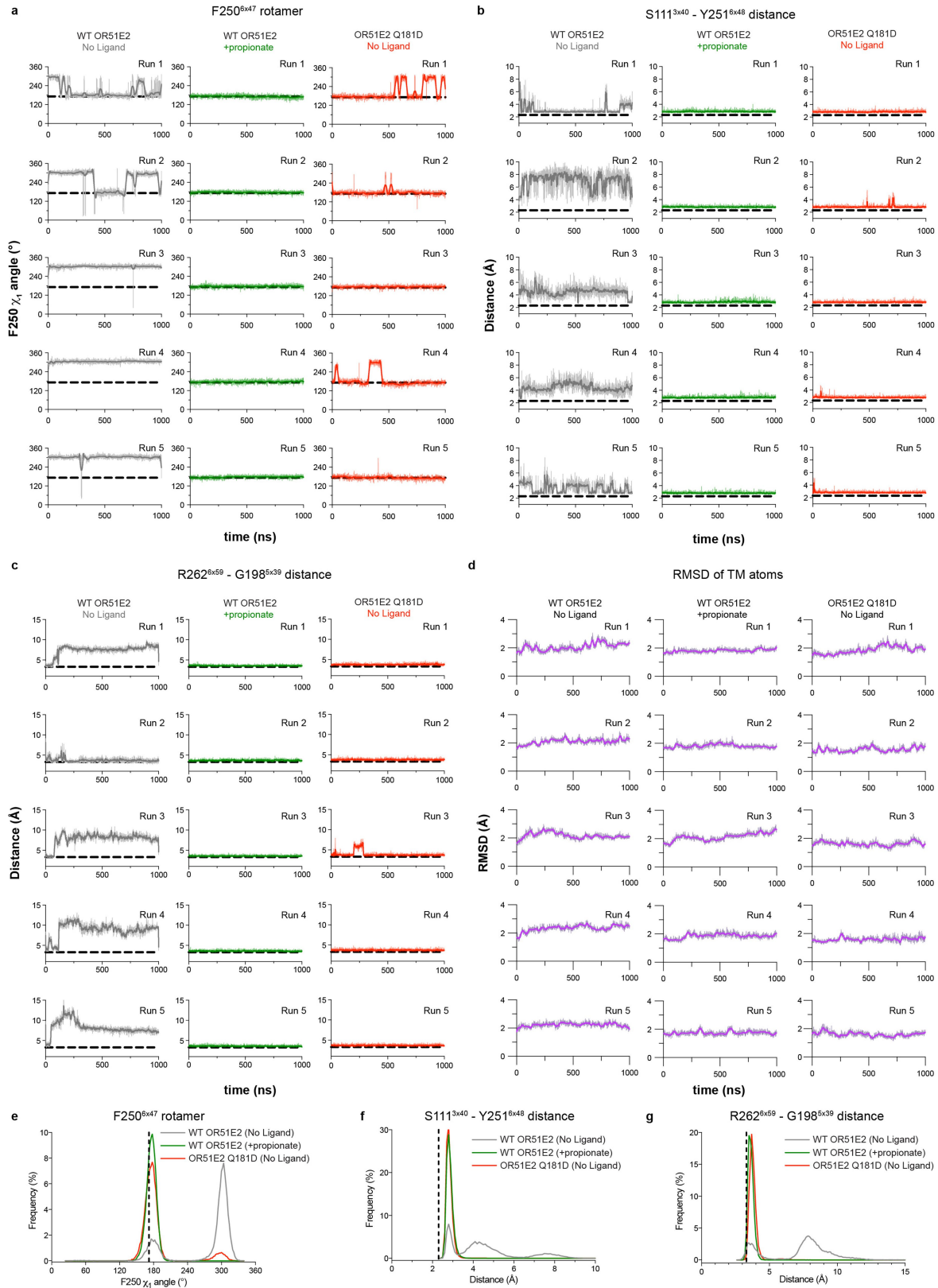


Extended Data Fig. 7 | Analysis of active state structure of OR51E2.

a) Structural comparison of G protein interaction for OR51E2 (green) and β2-adrenergic receptor (β2AR in blue, PDB code: 3SN6). b) Close-up views of intracellular loop 2 (ICL2) interaction with the Gα_s subunit shown in surface representation. c) interactions between residues in ICL2 and the αN and α5 helices of the Gα_s subunit. d) G protein-coupling region of OR51E2 is shown along with a weblogo (right) highlighting conservation of key residues for all

human ORs. e) Residues that participate in the extended interaction hydrogen bonding network between TM3, TM4, TM5, and TM6 are conserved in human Class I ORs, but not in Class II ORs. f,g) The percentage of receptors harboring a given amino acid at each position are shown for all human Class I and Class II ORs at the G protein-coupling region and connector regions. OR51E2 residues at each position are indicated by a black box.

Article



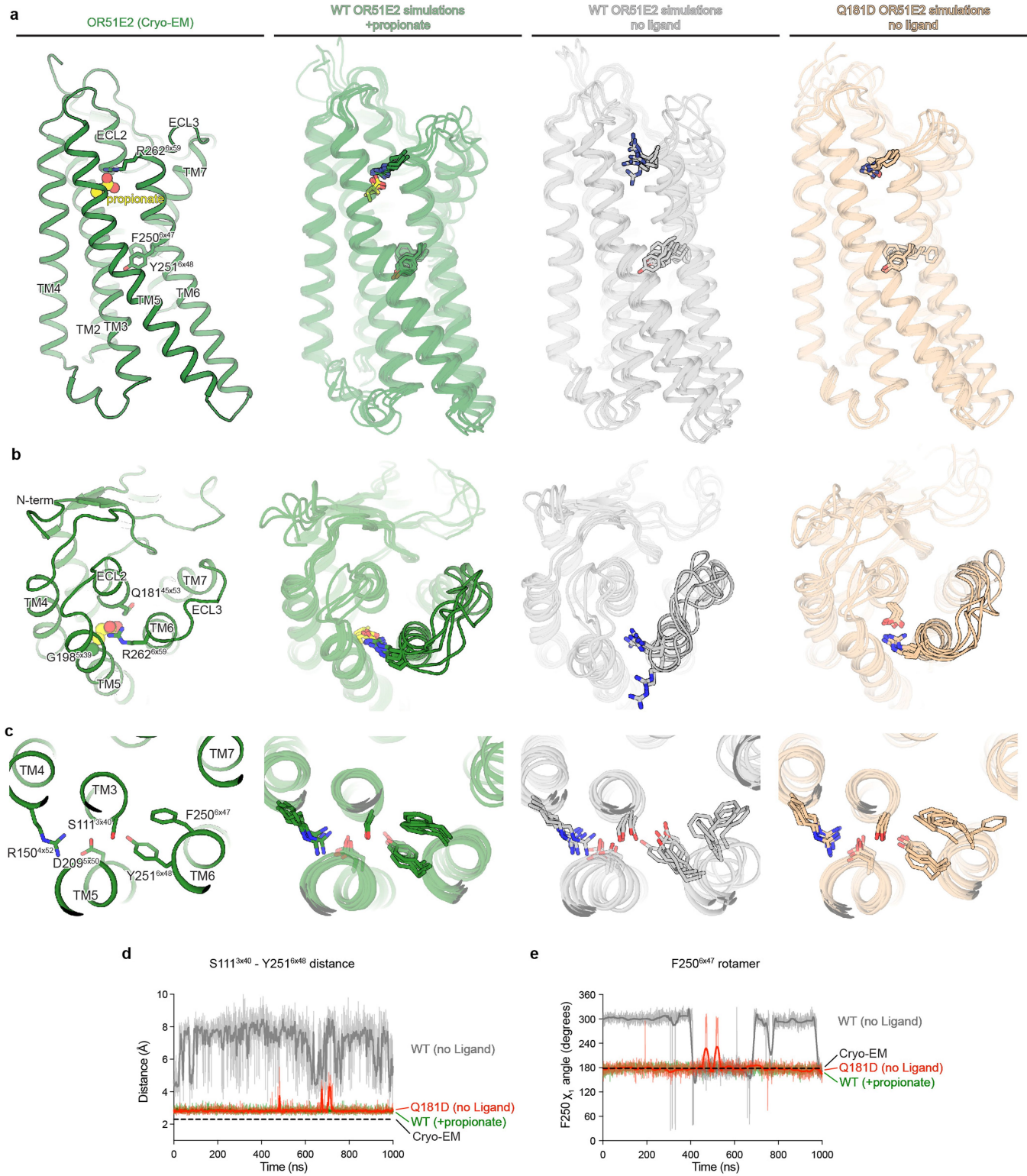
Extended Data Fig. 8 | See next page for caption.

Extended Data Fig. 8 | OR51E2 molecular dynamics simulation trajectories.

a–c) Simulation trajectories for WT and Q181^{45×53}D OR51E2 are shown in a–c. Five independent runs at different velocities are shown for each condition (top to bottom). **a)** F250^{6×47} χ_1 angle over replicate simulations. **b)** Minimum distance between oxygen atoms of the hydroxyl groups in the side chains of S111 and Y251^{6×48} over replicate simulations. **c)** Minimum distance between R262^{6×59} sidechain atoms and G198^{5×39} mainchain atoms (excluding the hydrogens) for replicate simulations. **d)** Root-mean-square deviation (RMSD) values for TM backbone atoms in the transmembrane helices (see Methods) calculated with reference to the equilibrated structure of the no ligand and propionate bound

OR51E2 simulations, as well as for simulations of Q181^{45×53}D OR51E2 from 5 independent MD simulation replicates (top to bottom). Thick traces represent smoothed values with an averaging window of 8 nanoseconds; thin traces represent unsmoothed values. **e–f)** Aggregate frequency distributions are shown for F250^{6×47} χ_1 angle (**e**), minimum distance between heavy atoms of the hydroxyl groups of S111^{3×40} and Y251^{6×48} (**f**), and minimum distance between R262^{6×59} sidechain heavy atoms and G198^{5×39} main chain heavy atoms (excluding hydrogens) (**g**) using all five simulation replicates for each condition.

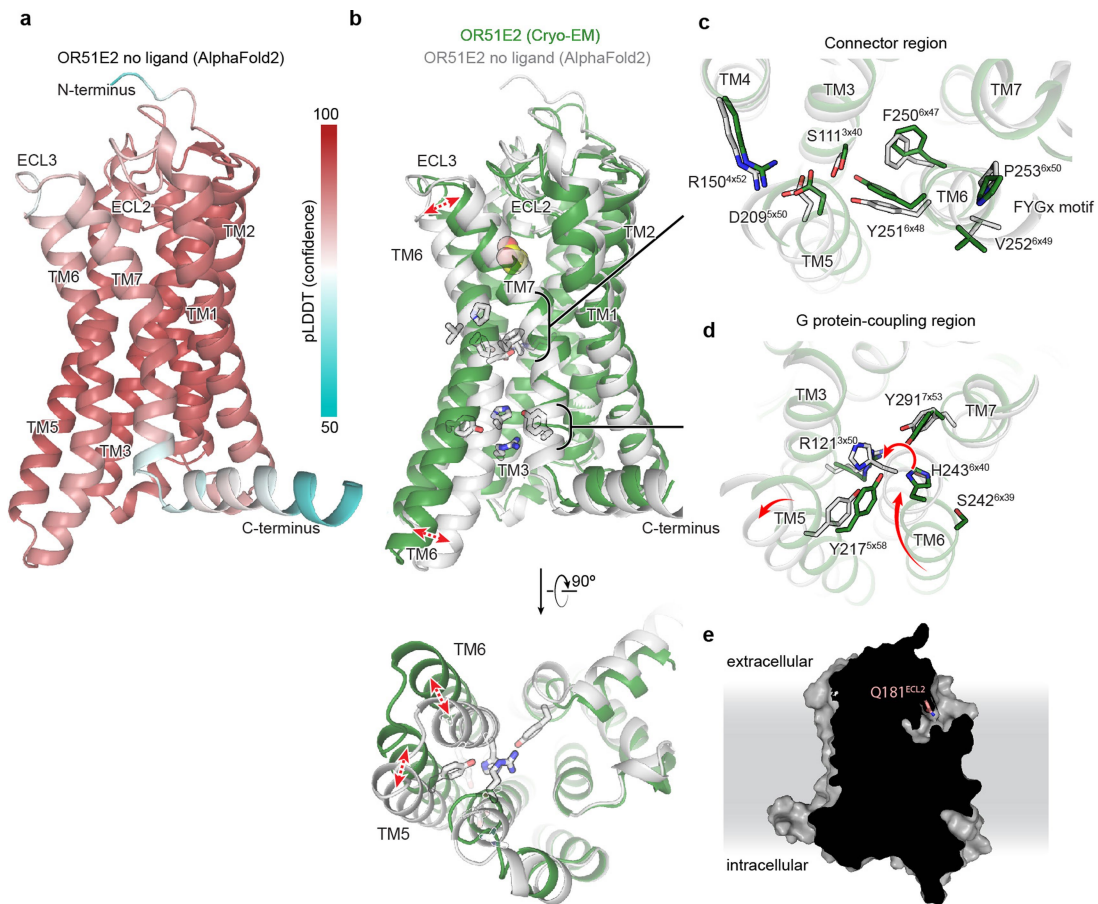
Article



Extended Data Fig. 9 | Molecular dynamics snapshots of OR51E2.

a) Comparison of cryo-EM structure of propionate-bound OR51E2 with representative snapshots from simulations of WT OR51E2 with propionate, WT OR51E2 without ligand, and Q181⁴⁵_x⁵³D OR51E2 without ligand. Notably, OR51E2 does not transition to the inactive conformation in any of these simulations. **b)** Close-up views of OR51E2 binding site and ECL3 region in the cryo-EM structure and simulations. In propionate-bound MD simulations of WT OR51E2, R262⁶_x⁵⁹ persistently forms an ionic interaction with propionate. In simulations of WT OR51E2 with propionate removed, R262⁶_x⁵⁹ is flexible. Introduction of Asp in position 45_x⁵³ (Q181⁴⁵_x⁵³D) stabilizes R262⁶_x⁵⁹ in an active-like state by a direct ionic interaction. **c)** Close-up views of OR51E2 connector region shows

increased flexibility of WT OR51E2 simulated without propionate. This flexibility is decreased for the Q181⁴⁵_x⁵³D mutant. In **a-c**, displayed snapshots are the last 1000th ns snapshots from each simulation replicate. **d,e)** Molecular dynamics trajectories from representative simulations to highlight structural organization of connector region. **d)** Minimum distance between S111³_x⁴⁰ and Y251⁶_x⁴⁸ hydroxyl groups is comparable for Q181⁴⁵_x⁵³D and propionate-bound WT OR51E2. **e)** Rotamer angle of F250⁶_x⁴⁷ is comparable for Q181⁴⁵_x⁵³D and propionate-bound WT OR51E2. Simulations were performed with or without propionate over the course of 1000 ns (see Extended Data Fig. 8 for replicates of simulation trajectories). Thick traces represent smoothed values with an averaging window of 8 nanoseconds; thin traces represent unsmoothed values.



Extended Data Fig. 10 | AlphaFold2 model of OR51E2. **a)** AlphaFold2 predicted structure of OR51E2. The pLDDT confidence metric is shown highlighting relatively high confidence in the transmembrane regions and extracellular loops. **b)** AlphaFold2 predicted structure of unbound OR51E2 (gray) superimposed onto the experimentally determined structure of propionate-bound OR51E2 in the active state (green cartoon and yellow

spheres). In the AlphaFold2 model, TM6 is inwardly displaced compared to the active structure. Closeup views of **(c)** the Connector region and **(d)** the G protein-coupling region are provided. **e)** Slice through surface representation of AlphaFold2 predicted OR51E2, suggests solvent accessibility of the ligand binding site in the inactive state.

Article

Extended Data Table 1 | Cryo-EM data collection, refinement, and validation statistics

Propionate-bound OR51E2-G_s	
EMDB: Full map	EMD-28896
EMDB: 7TM map	EMD-28900
RCSB PDB: Model	8F76
Data collection	
Microscope	Thermo Scientific Krios G3i
Detector	Gatan K3 with Gatan
Voltage (kV)	300
Magnification	105,000
Defocus range (μm)	-1.0 to -2.1
Pixel size, physical (\AA)	0.81
Total exposure ($e^-/\text{\AA}^2$)	50
Frame exposure ($e^-/\text{\AA}^2/\text{frame}$)	0.833
Images, number of	16,113
Frames/image, number of	60
Initial particles, number of	7,875,501
Final particles, number of	204,438
Symmetry imposed	C1
Map sharpening, <i>B</i> factor (\AA^2)	
Full map	-140.2
7TM map	-162.8
Map resolution, masked (\AA)	
Full map	3.1
7TM map	3.2
FSC threshold	0.143
Refinement	
Initial model used (AlphaFold code)	Q9H255
Model resolution (\AA)	3.2
FSC threshold	0.5
Model composition	
Chains	6
Non-hydrogen atoms	8,176
Protein residues	1,038
Ligands	1
<i>B</i> factors (\AA^2)	
Protein	37.96
Ligand	38.56
R.m.s. deviations	
Bond length (\AA)	0.005
Bond angles ($^\circ$)	0.873
Validation	
MolProbity score	1.51
Clash score	5.64
EMRinger score	3.50
Rotamer outliers (%)	0
Ramachandran plot	
Favored (%)	96.76
Allowed (%)	3.24
Disallowed (%)	0.00

Extended Data Table 2 | Expression and pharmacodynamic constants for OR51E2 variants

Surface expression (mean)	<i>Propionate activity in GloSensor cAMP assay</i>				Activity index (Emax * pEC ₅₀)
	EC ₅₀ (mM, mean)	pEC ₅₀ (-log M, mean ± S.E.M.)	Emax (mean ± S.E.M.)		
WT	8,490	0.824	3.08 ± 0.053	3.24 ± 0.049	9.98
H104A	4,130	17.1	1.77 ± 0.77	1.74 ± 0.63	3.08
S111A	112	n.r.	n.r.	n.r.	n.r.
R121A	192	n.r.	n.r.	n.r.	n.r.
R150A	163	n.r.	n.r.	n.r.	n.r.
F155A	8,700	12.3	1.91 ± 0.77	2.51 ± 0.099	4.79
L158A	5,250	1.6	2.8 ± 0.42	3.05 ± 0.43	8.53
H180A	4,570	n.r.	n.r.	n.r.	n.r.
Q181A	7,340	12.4	1.91 ± 0.32	2.68 ± 0.49	5.11
Q181D	9,140	38.9	1.41 ± 0.12	2.59 ± 0.25	3.65
Q181E	8,750	n.r.	n.r.	n.r.	n.r.
Q181N	4,910	3.9	2.41 ± 0.11	1.15 ± 0.016	2.77
G198A	5,960	n.r.	n.r.	n.r.	n.r.
I202A	9,730	13.7	1.86 ± 0.050	2.25 ± 0.060	4.2
D209A	112	n.r.	n.r.	n.r.	n.r.
Y217A	97.6	n.r.	n.r.	n.r.	n.r.
S242A	10,300	0.615	3.21 ± 0.080	3.48 ± 0.071	11.2
H243A	260	0.459	3.34 ± 0.095	1.39 ± 0.015	4.64
F250H	2,420	4.12	2.39 ± 0.036	3.01 ± 0.066	10.2
F250Y	3,450	0.423	3.37 ± 0.096	2.68 ± 0.039	6.38
Y251A	114	n.r.	n.r.	n.r.	n.r.
Y251F	1,500	4.72	2.33 ± 0.031	2.39 ± 0.029	5.56
Y251H	254	n.r.	n.r.	n.r.	n.r.
V252A	6,610	1.01	3.00 ± 0.085	2.97 ± 0.076	8.91
P253A	1,460	5.53	2.26 ± 0.05	2.32 ± 0.047	5.23
S258A	7,230	n.r.	n.r.	n.r.	n.r.
R262A	9,290	n.r.	n.r.	n.r.	n.r.
Y291A	3,080	1.4	2.85 ± 0.042	2.50 ± 0.031	7.13
mock	49.4	n.r.	n.r.	n.r.	n.r.

n.r. = no response (fit R² < 0.90)

Article

Extended Data Table 3 | Pharmacodynamic constants for fatty acid series at OR51E2 variants

	EC ₅₀ (μM, mean)	pEC ₅₀ (-log M, mean ± S.E.M.)	Emax (mean ± S.E.M.)	Activity index (Emax * pEC ₅₀)
WT OR51E2				
<i>Acetate (C2)</i>	1,360	2.87 ± 0.05	4.35 ± 0.07	12.5
<i>Propionate (C3)</i>	1,404	2.85 ± 0.06	4.52 ± 0.09	12.9
<i>Butyrate (C4)</i>	8,737	2.06 ± 0.33	2.85 ± 0.90	5.9
<i>Pentanoate (C5)</i>	n.r.	n.r.	n.r.	n.r.
<i>Hexanoate (C6)</i>	n.r.	n.r.	n.r.	n.r.
<i>Heptanoate (C7)</i>	n.r.	n.r.	n.r.	n.r.
<i>Octanoate (C8)</i>	n.r.	n.r.	n.r.	n.r.
<i>Nonanoate (C9)</i>	n.r.	n.r.	n.r.	n.r.
<i>Decanoate (C10)</i>	n.r.	n.r.	n.r.	n.r.
OR51E2 - F155A				
<i>Acetate (C2)</i>	28,800	1.54 ± 0.16	1.94 ± 0.16	2.98
<i>Propionate (C3)</i>	9,130	2.04 ± 0.59	2.86 ± 0.081	5.83
<i>Butyrate (C4)</i>	5,260	2.28 ± 0.21	2.28 ± 0.33	5.19
<i>Pentanoate (C5)</i>	7,290	2.14 ± 0.24	2.96 ± 0.67	6.33
<i>Hexanoate (C6)</i>	543	3.27 ± 0.045	3.46 ± 0.065	11.3
<i>Heptanoate (C7)</i>	29.8	4.53 ± 0.020	3.99 ± 0.023	18.1
<i>Octanoate (C8)</i>	5.46	5.26 ± 0.028	4.56 ± 0.032	24.0
<i>Nonanoate (C9)</i>	12.1	4.92 ± 0.074	3.22 ± 0.051	15.8
<i>Decanoate (C10)</i>	n.r.	n.r.	n.r.	n.r.
OR51E2 - L158A				
<i>Acetate (C2)</i>	15,300	1.82 ± 0.087	2.14 ± 0.092	3.90
<i>Propionate (C3)</i>	1,300	2.89 ± 0.10	2.70 ± 0.081	7.80
<i>Butyrate (C4)</i>	2,890	2.54 ± 0.056	4.28 ± 0.22	10.9
<i>Pentanoate (C5)</i>	7,380	2.13 ± 0.13	4.38 ± 0.69	9.33
<i>Hexanoate (C6)</i>	859	3.07 ± 0.042	4.78 ± 0.12	14.7
<i>Heptanoate (C7)</i>	1,380	2.86 ± 0.059	2.82 ± 0.10	8.08
<i>Octanoate (C8)</i>	n.r.	n.r.	n.r.	n.r.
<i>Nonanoate (C9)</i>	n.r.	n.r.	n.r.	n.r.
<i>Decanoate (C10)</i>	n.r.	n.r.	n.r.	n.r.

n.r. = no response (fit R² < 0.90)

Reporting Summary

Nature Research wishes to improve the reproducibility of the work that we publish. This form provides structure for consistency and transparency in reporting. For further information on Nature Research policies, see our [Editorial Policies](#) and the [Editorial Policy Checklist](#).

Statistics

For all statistical analyses, confirm that the following items are present in the figure legend, table legend, main text, or Methods section.

n/a Confirmed

- The exact sample size (n) for each experimental group/condition, given as a discrete number and unit of measurement
- A statement on whether measurements were taken from distinct samples or whether the same sample was measured repeatedly
- The statistical test(s) used AND whether they are one- or two-sided
Only common tests should be described solely by name; describe more complex techniques in the Methods section.
- A description of all covariates tested
- A description of any assumptions or corrections, such as tests of normality and adjustment for multiple comparisons
- A full description of the statistical parameters including central tendency (e.g. means) or other basic estimates (e.g. regression coefficient) AND variation (e.g. standard deviation) or associated estimates of uncertainty (e.g. confidence intervals)
- For null hypothesis testing, the test statistic (e.g. F , t , r) with confidence intervals, effect sizes, degrees of freedom and P value noted
Give P values as exact values whenever suitable.
- For Bayesian analysis, information on the choice of priors and Markov chain Monte Carlo settings
- For hierarchical and complex designs, identification of the appropriate level for tests and full reporting of outcomes
- Estimates of effect sizes (e.g. Cohen's d , Pearson's r), indicating how they were calculated

Our web collection on [statistics for biologists](#) contains articles on many of the points above.

Software and code

Policy information about [availability of computer code](#)

Data collection SerialEM 3.8

Data analysis GraphPad Prism 9.0, Phenix 1.19, Coot 0.9.2, MolProbity 4.5, ChimeraX 1.25, PyMOL 2.5, cryoSPARC 3.2, Relion 3.0, MotionCor2, UCSF pyEM v0.5, AlphaFold2, Flowjo v10.8.1, GROMACS 2021, OPM, VMD 1.9.3, Maestro v13.0.135, ClustalX/ClustalW 2.1, jalview v2.11.1.5, Biostrings 2.66.0, seqinr 4.2-23, ape 5.6-2, ggtree 3.6.2, R studio v 202.07.01

For manuscripts utilizing custom algorithms or software that are central to the research but not yet described in published literature, software must be made available to editors and reviewers. We strongly encourage code deposition in a community repository (e.g. GitHub). See the Nature Research [guidelines for submitting code & software](#) for further information.

Data

Policy information about [availability of data](#)

All manuscripts must include a [data availability statement](#). This statement should provide the following information, where applicable:

- Accession codes, unique identifiers, or web links for publicly available datasets
- A list of figures that have associated raw data
- A description of any restrictions on data availability

Coordinates for propionate OR51E2-Gs have been deposited in the RCSB PDB under accession code 8F76 . EM density maps for OR51E2-Gs and the 7TM domain of OR51E2 have been deposited in the Electron Microscopy Data Bank under accession codes EMD-28896, and EMD-28900, respectively. The molecular dynamics simulation trajectories for apo OR51E2, OR51E2 bound to propionate, and OR51E2-Q18145x53D mutant have been deposited in the GPCRdb database under access codes 1244, 1245, and 1246, respectively. This manuscript makes use of RCSB PDB accession codes 3SN6, 4LDO, and 6FUU.

Field-specific reporting

Please select the one below that is the best fit for your research. If you are not sure, read the appropriate sections before making your selection.

- Life sciences Behavioural & social sciences Ecological, evolutionary & environmental sciences

For a reference copy of the document with all sections, see nature.com/documents/nr-reporting-summary-flat.pdf

Life sciences study design

All studies must disclose on these points even when the disclosure is negative.

Sample size	For cryo-EM studies, the data size was limited by available instrument time and relative particle density on cryo-EM grids. For signaling studies, we used a sample size of 3-4 to enable repeatability and to control for biological variance typical in biochemical assays, with a minimum of two measurements per tested concentration. For molecular dynamics simulations, five independent replicates were performed to control for variance in initial starting conditions.
Data exclusions	No datapoints were excluded from analysis.
Replication	Biochemical assays were replicated 2 or 3 times (as indicated), with identical results. The structural biology approaches represent ensemble averages, and the individual experiments were not repeated, as is common and accepted practice in the field. Data processing approaches were replicated and assessed with well-established approaches as outlined in the Methods section.
Randomization	Randomization was not relevant to the experiments in our study as the assays don't have unknown covariates. For example, when we compare wild-type to mutant OR51E2 in signaling studies, there is no feasible unknown covariate that we can minimize by randomizing experimental units.
Blinding	Blinding was not relevant to the experiments in our study since no subjective allocation was involved.

Reporting for specific materials, systems and methods

We require information from authors about some types of materials, experimental systems and methods used in many studies. Here, indicate whether each material, system or method listed is relevant to your study. If you are not sure if a list item applies to your research, read the appropriate section before selecting a response.

Materials & experimental systems		Methods	
n/a	Involved in the study	n/a	Involved in the study
<input type="checkbox"/>	<input checked="" type="checkbox"/> Antibodies	<input checked="" type="checkbox"/>	<input type="checkbox"/> ChIP-seq
<input type="checkbox"/>	<input checked="" type="checkbox"/> Eukaryotic cell lines	<input checked="" type="checkbox"/>	<input type="checkbox"/> Flow cytometry
<input checked="" type="checkbox"/>	<input type="checkbox"/> Palaeontology and archaeology	<input checked="" type="checkbox"/>	<input type="checkbox"/> MRI-based neuroimaging
<input checked="" type="checkbox"/>	<input type="checkbox"/> Animals and other organisms		
<input checked="" type="checkbox"/>	<input type="checkbox"/> Human research participants		
<input checked="" type="checkbox"/>	<input type="checkbox"/> Clinical data		
<input checked="" type="checkbox"/>	<input type="checkbox"/> Dual use research of concern		

Antibodies

Antibodies used	M1-FLAG antibody (made in house using commercially available hybridoma HB-9259 sold via ATCC). Protein C antibody (made in house using commercially available hybridoma HB-9892 sold via ATCC). Anti-rhodopsin 4D2 antibody obtained from Sigma-Aldrich (MABN15) used at a dilution of 1:400 (v/v). Phycoerythrin-conjugated donkey anti-mouse F(ab')2 fragment antibody (Jackson Immunologicals: 715-115-150) used at a dilution of 1:200 (v/v).
Validation	Protein C antibody was purified over its respective antigen peptide, which was also used to validate binding. M1-FLAG antibody was purified over its respective antigen peptide, which was also used to validate binding. Anti-rhodopsin 4D2 antibody and Phycoerythrin-conjugated donkey anti-mouse F(ab')2 fragment antibody were validated by their respective manufacturers as indicated at these links: https://www.sigmaaldrich.com/US/en/product/nmm/mabn15 https://www.jacksonimmuno.com/catalog/products/715-116-150

Eukaryotic cell lines

Policy information about [cell lines](#)

Cell line source(s)

Sf9 and Hi5 insect cells (Expression Systems), Expi293F cells (ThermoFisher), BL21 Rosetta Escherichia coli (UC Berkeley QB3 MacroLab), HEK293T cells (ATCC)

Authentication

Sf9, Hi5, and Expi293 cells were not authenticated. Duke DNA Analysis Facility conducted DNA profiling of HEK293T lab stock for polymorphic short tandem repeat (STR) markers using a GenePrint 10 (Promega) and confirmed shared profiles with the reference (ATCC CRL3216).

Mycoplasma contamination

Sf9, Hi5, and Expi293 cells were not tested for mycoplasma contamination. HEK293T cells tested negative for mycoplasma contamination.

Commonly misidentified lines
(See [ICLAC](#) register)

None